New Journal of Physics
The open-access journal for physics

Nodal domain statistics for quantum chaotic maps*

J P Keating, J Marklof and I G Williams[1,2]
School of Mathematics, University of Bristol, Bristol BS8 1TW, UK
E-mail: ian.williams@brunel.ac.uk

New Journal of Physics **10** (2008) 083023 (31pp)
Received 20 November 2007
Published 15 August 2008
Online at http://www.njp.org/
doi:10.1088/1367-2630/10/8/083023

Abstract. We study the statistical distribution of nodal domains in the eigenvectors of quantum chaotic maps in the semiclassical limit. For generic quantum maps, which are believed to behave statistically like random matrices, the nodal domains are described by an uncorrelated critical percolation model. This leads to predictions for the distribution of the number, size and fractal dimension of the nodal domains, which are tested numerically. Furthermore, we find that the corresponding nodal lines can be modelled by stochastic Loewner evolution (SLE) with parameter κ close to 6. Interestingly, the percolation model and SLE are also found to describe the statistical properties of the nodal domains for the quantum cat map, which is non-generic in that its spectral statistics do not fall into any of the random matrix universality classes.

Contents

* Dedicated to the memory of Charles Schmit.

[1] Present address: Department of Mathematical Sciences, Brunel University, West London, Uxbridge UB8 3PH, UK.

[2] Author to whom any correspondence should be addressed.

1. Introduction

The quantum eigenfunctions of classically chaotic systems have a remarkably complex morphology. Statistically, their fluctuations are believed to be described in the semiclassical limit by Berry's random wave model [1], which leads directly to predictions for local measures, such as value distributions and correlations on length-scales that are of the order of the de Broglie wavelength. More generally, the random wave model describes the statistical properties of waves in complex geometries, with applications ranging from optics to the cosmic microwave background.

One natural way to analyse the morphology of real, scalar eigenfunctions, for example the eigenfunctions of time-reversal-symmetric systems, is via their separation into *nodal domains*—connected regions in which the eigenfunctions have constant sign, separated from each other by surfaces where the eigenfunctions vanish. This is a particularly useful way of visualizing patterns in two-degree-of-freedom systems, where the nodal sets are lines separating two-dimensional nodal domains.

There has recently been considerable interest in the statistical properties of nodal domains in two-degree-of-freedom billiard systems. It was shown in [2] that fluctuations in the number of nodal domains in different eigenfunctions have a normal distribution in classically chaotic systems, and as such are different from those in classically separable systems. For chaotic billiards, a critical percolation model based on Berry's random wave model was proposed in [3], and found to give accurate predictions for the nodal domain statistics. It predicts, for example, the values of critical exponents associated with the area distribution and fractal dimensions of the nodal domains. The statistics of the area-to-perimeter ratio of the nodal domains was considered in [4], where the percolation model was found to describe the larger domains.

Despite the apparent success of the percolation model, it is unsatisfying in some ways. A systematic derivation of the percolation model for billiard-type systems is still lacking. Furthermore, a measure proposed by Foltin *et al* [5], relating to the distance of a nodal line from a given reference curve, has been shown to have a different scaling behaviour to that expected from the uncorrelated percolation model; and recent work by Aronovitch and Smilansky [6] shows that the intersections of nodal lines with a reference curve have different statistics to those which would be expected for a short-ranged percolation model. On the other hand, Bogomolny and Schmit [7] have argued that the oscillations in the autocorrelation of random waves are sufficient to justify the use of short-ranged percolation models.

With the aim of clarifying the connection between chaotic systems and percolation models, we analyse here a critical percolation model for another class of model quantum chaotic systems, namely quantum maps. For these we show that the percolation model follows directly from the standard conjecture that generic quantum maps behave statistically like random matrices [8], with no additional assumptions. Indeed, it follows from a weaker hypothesis implied by the random-matrix conjecture. We are able to probe the percolation model for maps numerically in significantly greater detail than has been achieved for billiard systems. In the case of a family of maps for which the random matrix conjecture holds, the perturbed cat maps, we find striking confirmation. The fact that the eigenfunctions of quantum maps are so well described by a critical percolation model motivates the question: to what extent are they conformally invariant? In this context, we show that their nodal lines are well modelled by paths generated by stochastic Loewner evolution (SLE) with a diffusion constant close to 6. We also explore these connections for a family of maps, the cat maps, which are nongeneric,

in that they possess arithmetical (i.e. number theoretical) symmetries and so are not expected to be described by random matrix theory. We find that the connection to percolation theory and SLE is surprisingly robust in this context. The arithmetical symmetries render these maps particularly amenable to rigorous analysis, and our results suggest that it might be interesting to explore their nodal domains in this way.

For generic systems, which we expect to be described by random matrix theory, our preliminary results and conclusions concerning the percolation model and the connection with SLE were reported briefly in [9]. Here we present significantly more data in support of our conclusions, and in particular, provide a new method for analysing them that considerably improves the accuracy of the estimate of the diffusion constant in the comparison with SLE. In addition, we provide full details of the calculations outlined in [9]. The results we present for the cat maps, which are representative arithmetical systems, are also new.

This paper is structured as follows. In the next section, we will outline the percolation model for maps introduced in [9] and describe the quantum perturbed cat maps, which will be the basis of our numerical computations. In section 3, we discuss some numerical tests of the percolation model, and sections 4 and 5 discuss results related to conformal invariance and SLE that support the links proposed in [9].

2. The percolation model for maps

We consider dynamical systems acting on a periodic phase space. If the configuration space is L-dimensional, points in the phase space are specified by the coordinate

$$\mathbf{x} = \begin{pmatrix} \mathbf{q} \\ \mathbf{p} \end{pmatrix},$$

where $\mathbf{q}$ and $\mathbf{p}$ are the L dimensional position and momentum, respectively, and $\mathbf{x} \in \mathbb{T}^{2L}$. Maps of this phase space will have quantum eigenfunctions that are periodic, up to phases, in $\mathbf{x}$. With the requirement that all of these phases are zero, Planck's constant is restricted to have values $h = 1/N$, where N is an integer, and the eigenfunctions are of the form

$$|\Psi\rangle = \sum_{\mathbf{Q} \in \square_N} \Psi(\mathbf{Q}) |\mathbf{Q}\rangle, \tag{1}$$

where $\square_N = (\mathbb{Z} \setminus N\mathbb{Z})^L$, and

$$\langle \mathbf{q} | \mathbf{Q} \rangle = \sum_{\mathbf{n} \in \mathbb{Z}^L} \delta^L \left(\mathbf{q} - \frac{\mathbf{Q}}{N} - \mathbf{n} \right). \tag{2}$$

The Hilbert space is N^L dimensional, and the quantum map is a unitary $N^L \times N^L$ matrix in the basis consisting of the $\Psi(\mathbf{Q})$ [10]. It will be our aim to use the values of the components of Ψ to define a percolation model, by considering the discrete points in the support of the eigenfunction to correspond with sites in a site percolation model. A site will be considered as *occupied* in the event that the (real) eigenfunction is positive at this point.

We now use the key observation of [11]: in the case where the classical map is chaotic and time reversal symmetric, the statistics of both the eigenvalues and eigenvectors of the quantized map are expected to be given by the circular orthogonal ensemble (COE) of random matrices.

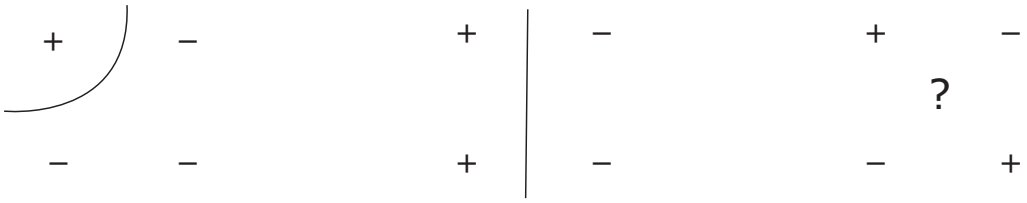

Figure 1. Determining the connectivity of the nodal domains.

In particular, the distribution of normalized eigenvectors is uniform over the unit sphere in N^L dimensions under this assumption, that is, its probability density is

$$\mathcal{P}(\Psi) = \delta\left(1 - \sum_{\mathbf{Q}\in\square_N} \Psi(\mathbf{Q})^2\right). \tag{3}$$

The important feature of (3) for our purposes is its symmetry under the transformation $\Psi(\mathbf{Q}_i) \to -\Psi(\mathbf{Q}_i)$ for any single component $\mathbf{Q}_i \in \square_N$. This immediately suggests that $\Psi(\mathbf{Q}_i) > 0$ with probability $1/2$, independently of all other components. Hence, one can define an uncorrelated percolation model for the nodal domains. Note that the independence here is an immediate consequence of (3), rather than an assumption, as it is in the Bogomolny–Schmit theory [3, 7].

In the one-dimensional case, this percolation model was introduced by Keating *et al* [11]. The eigenfunctions are supported at points j/N, and are periodic under $j \to j+N$. The eigenfunctions then take the form of a periodic sequence of numbers $\Psi(j)$, and the number of nodal domains is equal to the number of sign changes in this sequence. With this definition of the nodal domains, one can calculate explicitly the distribution of the number of nodal domains. It is just the binomial distribution. One-dimensional percolation models do not, however, exhibit critical behaviour, and as such this model cannot display the full range of behaviour apparent in the model of [3].

Here we consider a generalization of the percolation model of [11] to the case where the configuration space is two-dimensional. Care must be taken in choosing how the nodal domains are defined in this case. In figure 1, all possible configurations of four adjacent signs, up to rotations and sign inversions, are shown. There is an ambiguity in assigning the connectivity in the third case. We choose the convention (see [9]) that $\mathbf{Q}$ is connected to $\mathbf{Q}\pm\mathbf{e}_1$, $\mathbf{Q}\pm\mathbf{e}_2$ and $\mathbf{Q}\pm(\mathbf{e}_1+\mathbf{e}_2)$, where $\mathbf{e}_i$ denotes the ith basis vector. With this choice of connectivity one obtains a site percolation model on the triangular lattice, which is critical at site occupation probability $1/2$ [12].

This is only one of many possible definitions of the percolation model. We may, for example, deform the lattice by a transformation from the special linear group $\mathrm{SL}(2,\mathbb{Z})$. However, as a coordinate transformation the result of this is simply a unitary transformation of the basis $|\mathbf{Q}\rangle$, which leaves the COE invariant and as such has no effect on the expected eigenvector distribution.

In order to test the percolation model numerically, we consider quantizations of linear, symplectic maps of the form

$$\mathbf{x}_{n+1} = M\mathbf{x}_n \mod 1, \tag{4}$$

with

$$M = \begin{pmatrix} A & B \\ C & D \end{pmatrix}, \tag{5}$$

where A, B, C and D are nonsingular 2×2 matrices. This is a two-dimensional analogue of the cat maps used in [11]. In order to justify the COE assumption, we choose maps which are time-reversal symmetric and are *hyperbolic*. The hyperbolicity ensures that the maps are chaotic. The quantization of maps in $\mathrm{Sp}(4, \mathbb{Z})$ can be performed by a generalization of the Hannay–Berry method [10]. The resulting quantized map acts on the wavefunction expressed in the basis $|\mathbf{Q}\rangle$:

$$\Psi(\mathbf{Q}_2) = \sum_{\mathbf{Q}_1 \in \square_N} U_{\mathbf{Q}_2,\mathbf{Q}_1} \Psi(\mathbf{Q}_1), \tag{6}$$

where

$$U_{\mathbf{Q}_2,\mathbf{Q}_1} = \left(\frac{i}{N}\right)^{L/2} \sqrt{\det B} \exp\left(\frac{\mathrm{i}\pi}{N}\left[\mathbf{Q}_1 \cdot B^{-1}A \cdot \mathbf{Q}_1 + \mathbf{Q}_2 \cdot DB^{-1} \cdot \mathbf{Q}_2 - 2\mathbf{Q}_2 \cdot (B^t)^{-1} \cdot \mathbf{Q}_1\right]\right) \times \left\langle \exp\left(\mathrm{i}\pi\left[N\mathbf{m} \cdot B^{-1}A \cdot \mathbf{m} + 2\mathbf{Q}_1 \cdot B^{-1}A \cdot \mathbf{m} - 2\mathbf{Q}_2 \cdot (B^t)^{-1} \cdot \mathbf{m}\right]\right)\right\rangle_{\mathbf{m}}, \tag{7}$$

where the notation $\mathbf{v} \cdot V \cdot \mathbf{v}$ involving a vector $\mathbf{v}$ and square matrix V is to be understood as $\mathbf{v}^t V \mathbf{v}$ and $(\cdot)^t$ denotes the transpose. The notation $\langle \cdots \rangle_{\mathbf{m}}$ introduced in (7) denotes an average over all integer vectors $\mathbf{m}$. We give the derivation of this result in the appendix.

The map chosen for numerical studies must be symplectic. This gives six constraints on the matrix elements. In addition, one requires the map to be time-reversal symmetric. This implies

$$TMT = M^{-1}, \tag{8}$$

where T is the time-reversal operator

$$T = \begin{pmatrix} I & 0 \\ 0 & -I \end{pmatrix}, \tag{9}$$

which gives another five constraints. Hence, there are five free entries in the matrix. In addition to these constraints, the matrix is required to be hyperbolic, and must satisfy the quantizability conditions [13]

$$(AB^t)_{ii} = 0, \quad \mod 2, \quad i = 1, 2, \tag{10}$$

$$(CD^t)_{ii} = 0, \quad \mod 2, \quad i = 1, 2. \tag{11}$$

With these requirements, a computer search in MATHEMATICA was performed to find a suitable map. One example which we shall work with is the map given by the matrix

$$M = \begin{pmatrix} 2 & -2 & -2 & -1 \\ -2 & 6 & -1 & 0 \\ 16 & -39 & 2 & -2 \\ -39 & 94 & -2 & 6 \end{pmatrix}, \tag{12}$$

which has eigenvalues

$$\begin{aligned} &\lambda_1 = 0.0736202\ldots, \quad \lambda_2 = 0.561177\ldots, \\ &\tfrac{1}{\lambda_1} = 13.5832\ldots, \quad \tfrac{1}{\lambda_2} = 1.78197\ldots. \end{aligned} \tag{13}$$

It is clear from (12) that the averaging over integer vectors in (7) can be performed easily in this case, because $\det B = -1$, and consequently all $\mathbf{m}$ in the average are equivalent.

In the case of the cat maps, it is known [10, 14] that the quantum cat map is periodic up to a phase. This leads to non-generic eigenvalue statistics, which are inconsistent with the COE assumption. It has been shown [13] that this also applies to maps of the four-torus (i.e. when $L = 2$). To remedy this, we follow [11] in adding a nonlinear perturbation to the classical map. The map is perturbed to have the form $\rho \circ M \circ \rho$, where ρ is the following nonlinear shear in the momentum:

$$\rho \begin{pmatrix} q_1 \\ q_2 \\ p_1 \\ p_2 \end{pmatrix} = \begin{pmatrix} q_1 \\ q_2 \\ p_1 + \frac{k_1}{4\pi} \cos 2\pi q_1 \\ p_2 + \frac{k_2}{4\pi} \cos 2\pi q_2 \end{pmatrix}. \tag{14}$$

The perturbation is added in such a way as to keep the composite map time-reversal invariant. The quantization of (14) is derived in appendix A.3, and is found to be a diagonal matrix in the basis $|\mathbf{Q}\rangle$. Combining (7) with (A.59), the quantization of the perturbed map is given by

$$U_{\mathbf{Q},\mathbf{Q}'} = -\frac{1}{N} \exp\left[\frac{2\pi i}{N}\left(\mathbf{Q}\cdot\begin{pmatrix} 1 & -3 \\ -3 & 7 \end{pmatrix}\cdot\mathbf{Q} + \mathbf{Q}'\cdot\begin{pmatrix} 1 & -3 \\ -3 & 7 \end{pmatrix}\cdot\mathbf{Q}' + \mathbf{Q}'\cdot\begin{pmatrix} 0 & 1 \\ 1 & -2 \end{pmatrix}\cdot\mathbf{Q}\right)\right]$$
$$\times \exp\left[\frac{\mathrm{i}N}{4\pi}\left(k_1 \sin\frac{2\pi Q_1}{N} + k_1 \sin\frac{2\pi Q_1'}{N} + k_2 \sin\frac{2\pi Q_2}{N} + k_2 \sin\frac{2\pi Q_2'}{N}\right)\right]. \tag{15}$$

The time reversal symmetry can be seen clearly in (15) from the invariance under $\mathbf{Q} \leftrightarrow \mathbf{Q}'$. The quantized map in (15) will be the basis of most of the numerical results presented in the sequel. We will also present some results for the unperturbed cat maps ($k_1 = k_2 = 0$) for comparison.

The hyperbolic toral automorphisms are structurally stable [15]—the periodic orbits are stable under perturbations. Consider perturbations of the map M. If we choose a constant a such that

$$|\lambda_i| < a, \quad i = 1, 2, \tag{16}$$

the perturbed map, written in the form $M + f$, is hyperbolic provided that

$$\max_{\mathbf{x}} \left(\frac{\left|\frac{\partial f}{\partial \mathbf{x}} \cdot \mathbf{x}\right|}{|\mathbf{x}|}\right) < 1 - a. \tag{17}$$

For the map (15), this criterion can be applied to give limits on the values of the perturbation parameters k_1 and k_2 such that the resulting map is hyperbolic. The domain where this is the case is shown in figure 2.

We shall also show some calculations for the alternative map given by the matrix

$$M = \begin{pmatrix} 1 & 2 & 2 & 1 \\ -1 & 5 & 1 & 1 \\ 4 & -10 & 1 & -1 \\ -10 & 32 & 2 & 5 \end{pmatrix} \tag{18}$$

with eigenvalues

$$\begin{aligned} &\lambda_1 = 0.11476\ldots, \quad \lambda_2 = 0.35505\ldots, \\ &\tfrac{1}{\lambda_1} = 8.7137\ldots, \quad \tfrac{1}{\lambda_2} = 2.8165\ldots. \end{aligned} \tag{19}$$

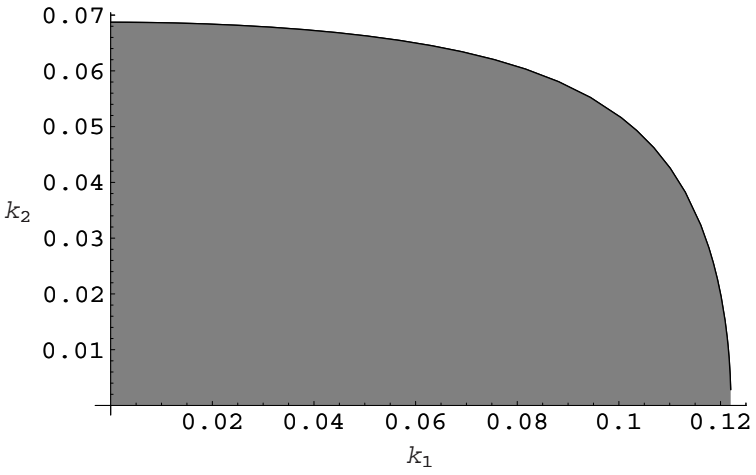

Figure 2. The limits on the size of the perturbation parameters k_1 and k_2 for map (15).

The perturbed map can be quantized as described above, with the resulting quantized perturbed map given by

$$U_{\mathbf{Q},\mathbf{Q}'} = \frac{\mathrm{i}}{N}\exp\left[\frac{\mathrm{i}\pi}{N}\left(\mathbf{Q}\cdot\begin{pmatrix}2 & -3\\ -3 & 8\end{pmatrix}\cdot\mathbf{Q}+\mathbf{Q}'\cdot\begin{pmatrix}2 & -3\\ -3 & 8\end{pmatrix}\cdot\mathbf{Q}'-2\mathbf{Q}'\cdot\begin{pmatrix}1 & -1\\ -1 & 2\end{pmatrix}\cdot\mathbf{Q}\right)\right]$$
$$\times\exp\left[\frac{\mathrm{i}N}{4\pi}\left(k_1\sin\frac{2\pi Q_1}{N}+k_1\sin\frac{2\pi Q_1'}{N}+k_2\sin\frac{2\pi Q_2}{N}+k_2\sin\frac{2\pi Q_2'}{N}\right)\right]. \qquad (20)$$

3. Numerical results

We are now equipped to study the nodal domain distribution for the eigenvectors of the quantum maps (15) and (20), representative examples of which are shown in figure 3. In this study, one may vary N and the perturbation parameters. When statistical averages are taken, they will be taken over all eigenvectors of a given map. A further averaging over parameters may also be taken, and this will be indicated in the text. We also show data for Monte Carlo simulations of percolation on a 61×61 lattice in order to check for finite-size effects

The main numerical tools in this study are the LAPACK package, which is used for the numerical diagonalization of the map (15) and the Hoshen–Kopelman algorithm introduced in [16], which is a fast method of counting the number of clusters.

3.1. Distribution of the total number of nodal domains

For any site percolation model, the number of clusters, which correspond to the nodal domains, is expected to have a simple asymptotic form as the number of sites, S, tends to infinity. This is given by [17]

$$n = n_c S + b + \mathrm{O}(S^{-1}). \qquad (21)$$

Here b is a universal constant, dependent only on the geometry of the boundary and the dimensionality of the underlying space, while n_c is dependent on the lattice model and the type

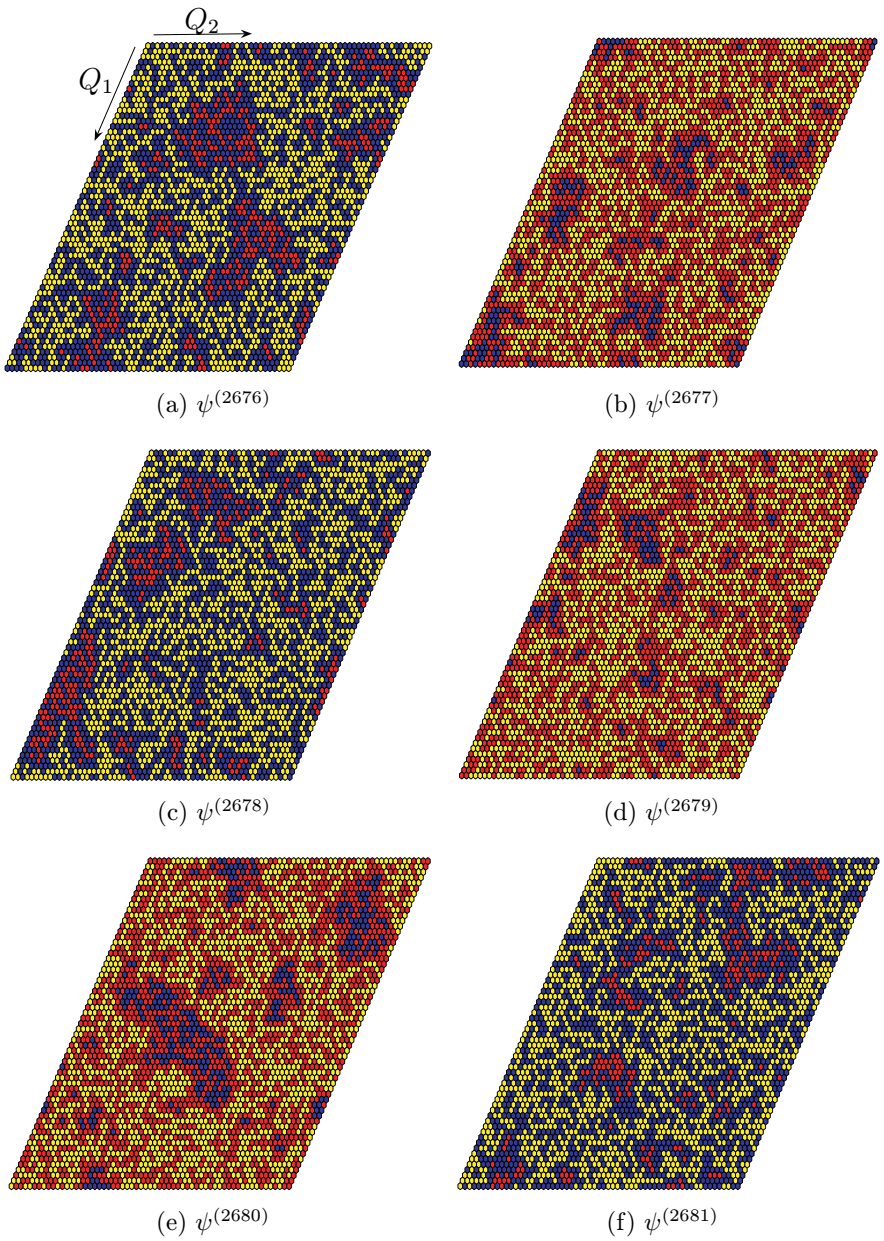

Figure 3. A sequence of typical quantum eigenvectors for the map (15) with $k_1 = 0.01$ and $k_2 = 0.02$. Each hexagonal face corresponds to one component of the eigenvector. The blue hexagons correspond to negative components and the red hexagons correspond to positive components. Two adjacent hexagons of the same colour lie in the same nodal domain. The largest nodal domain in each case is highlighted in yellow.

of percolation. In the geometry under consideration, the values of n_c and b have been calculated numerically by Monte Carlo methods [17]:

$$n_c = 0.0176255(5), \tag{22}$$

$$b = 0.8783(8). \tag{23}$$

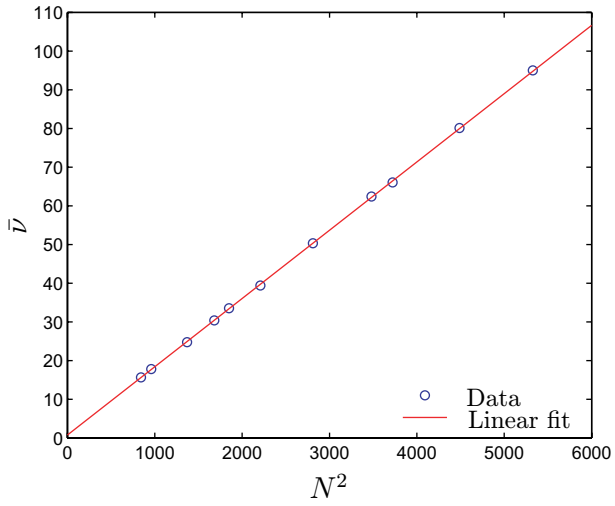

Figure 4. The dependence of $\bar{\nu}$ on N^2 with a fit to the predictions of (21) for the map (20) with $k_1 = 0.01$ and $k_2 = 0.01$. The linear fit gives values $n_c = 0.0176$ and $b = 0.7484$.

For fixed values of k_1 and k_2, we consider the dependence of the mean and variance of the number of nodal domains on N. The mean number of nodal domains, $\bar{\nu}$, is defined by

$$\bar{\nu} = \frac{1}{N^2} \sum_{i=1}^{N^2} \nu_i, \tag{24}$$

where ν_i denotes the number of nodal domains of the ith eigenvector. In figure 4, the behaviour of $\bar{\nu}$ is shown for map (20) with $k_1 = 0.01$ and $k_2 = 0.01$ as a function of the number of sites, N^2. By a least-squares linear fit we find $n_c^{\text{fit}} = 0.0176$ and $b^{\text{fit}} = 0.7484$ in this case. These values are in good agreement with the values in (22) and (23) computed by Ziff *et al* [17].

The variance of the number of nodal domains is defined for the quantum map eigenvectors by

$$\text{var}(\nu) = \frac{1}{N^2} \sum_{i=1}^{N^2} (\nu_i - \bar{\nu})^2, \tag{25}$$

and is expected to increase as $0.0309N^2$ from the numerical results of Ziff [17]. The computed values for map (20) with $k_1 = 0.01$ and $k_2 = 0.01$ are shown in figure 5. The linear fit gives a value of

$$\sigma_{\text{fit}}^2 = 0.0295N^2 + 2.80. \tag{26}$$

For the map given in equation (15), these calculations were repeated for several values of the perturbation parameters, and the value of the constant α in the equation $\text{var}(\nu) = \alpha N^2$ is shown in table 1, along with values for n_c and b. The average values calculated from table 1 are as follows:

$$n_c^{\text{fit}} = 0.0176, \quad b^{\text{fit}} = 0.9(1), \quad \alpha^{\text{fit}} = 0.0304(7).$$

The numbers in brackets denote the standard deviations in the data. The error in n_c is in the next digit. These mean values are consistent with the calculations for critical percolation given

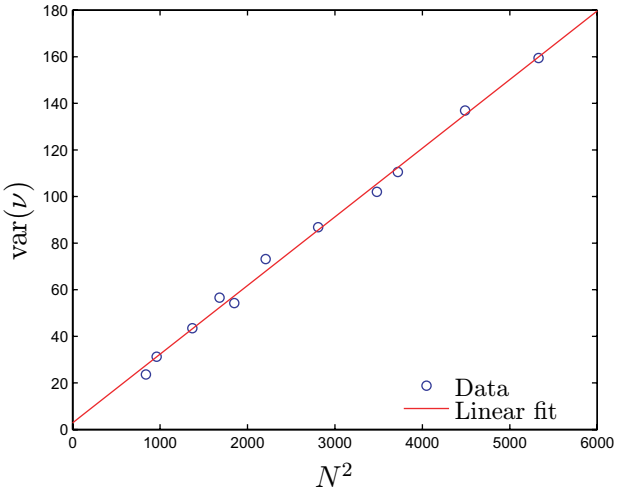

Figure 5. The computed variance, var(ν) for the quantum map (20) with $k_1 = 0.01$, $k_2 = 0.01$. The fit gives the behaviour $\mathrm{var}(\nu) = 0.0295N^2 + 2.80$.

in [17]. For comparison, our Monte Carlo simulations of uncorrelated percolation on small grids of dimension up to 61×61 resulted in the fit parameters $n_c = 0.0176$, $b = 0.964$ and $\alpha = 0.0292$.

3.2. Area distribution of nodal domains

The area distribution of the nodal domains is expected to have the following asymptotic form for clusters containing a large number of sites

$$n(a) \asymp a^{-\tau}, \tag{27}$$

where $\tau = 187/91$ is the Fisher exponent and the symbol $\asymp$ denotes that each side of the equation may be bounded by a constant multiple of the other side. This power law was tested for eigenvectors of the quantum map (15). We define $n_i(a)$ as the number of clusters containing a sites in the ith eigenvector. The average area distribution is then defined as

$$\bar{n}(a) := \frac{1}{N^2} \sum_{i=1}^{N^2} n_i(a). \tag{28}$$

The results for $k_1 = 0.01$ and $k_2 = 0.02$ are shown in figure 6. The data show good agreement with the expected power law behaviour apart from at small values of a, where the power law behaviour is not expected to hold.

It is appropriate to make a comment at this point about how much we may read into this apparent agreement. While the appearance of the power law scaling is encouraging, one cannot extract the value of the exponent from data covering few orders of magnitude. Ideally, one must examine the area distribution over a much larger range.

3.3. Fractal dimension of the nodal domains

The fractal dimension of critical percolation clusters is non-integer in the limit where the lattice size tends to infinity, corresponding to the limit $N \to \infty$ in our model. This was

Table 1. The mean and variance of the number of nodal domains for varying perturbation parameters.

k_1	k_2	b	n_c	α
0.01	0.02	0.9803	0.0175	0.0314
0.01	0.03	0.8910	0.0176	0.0309
0.01	0.04	0.9273	0.0176	0.0313
0.01	0.05	0.7920	0.0176	0.0302
0.02	0.01	0.8282	0.0176	0.0308
0.02	0.03	0.9536	0.0176	0.0310
0.02	0.04	0.0517	0.0175	0.0303
0.02	0.05	0.9550	0.0176	0.0319
0.03	0.01	0.8650	0.0175	0.0297
0.03	0.02	0.9069	0.0176	0.0303
0.03	0.04	1.1184	0.0175	0.0299
0.03	0.05	0.9354	0.0176	0.0296
0.04	0.01	0.9023	0.0176	0.0297
0.04	0.02	0.8214	0.0176	0.0300
0.04	0.03	0.9182	0.0176	0.0292
0.04	0.05	0.8049	0.0176	0.0300
0.05	0.01	0.7977	0.0176	0.0300
0.05	0.02	0.9098	0.0176	0.0304
0.05	0.03	0.8564	0.0176	0.0303
0.05	0.04	0.6117	0.0177	0.0310

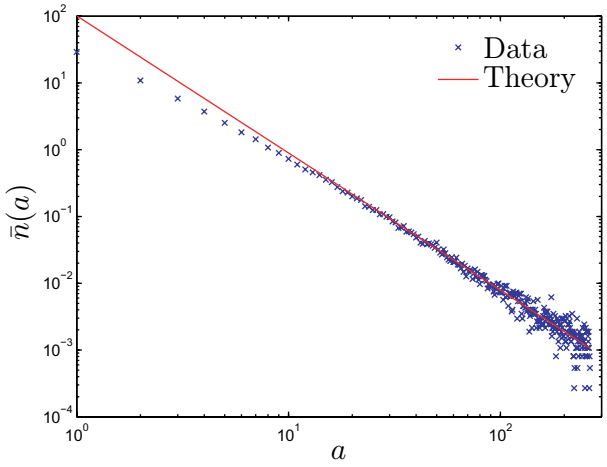

Figure 6. The calculated area distribution for map (15) with $N = 61$, $k_1 = 0.01$ and $k_2 = 0.02$. The straight line shows a power law decay with the theoretical value $\tau = 187/91$ predicted by percolation theory.

tested numerically for the eigenvectors of (15). We considered only the case $N = 61$ and for each eigenvector found a numerical estimate of the fractal dimension of the largest nodal domain.

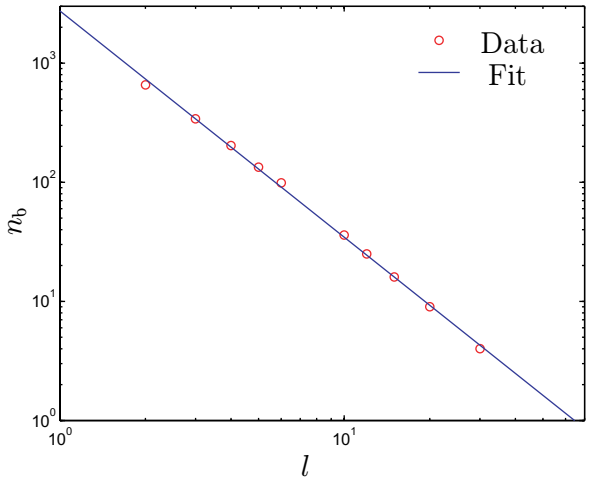

Figure 7. The computation of the fractal dimension for the largest nodal domain of the eigenvector of the map (15) with values $N = 61$, $k_1 = 0.05$ and $k_2 = 0.1$ and eigenvalue $\phi = -2.3524$. The computed value of the fractal dimension from the linear fit is $D^{\text{fit}} = 1.8998$.

In order to estimate the fractal dimension of the nodal domains, we use the box-counting algorithm [18, section 3.1]. A regular square grid with spacing l is superimposed over the nodal domain pattern, and the number of boxes, $n_b(l)$ intersected by the nodal domain is counted. The value of $n_b(l)$ is then expected to vary according to the formula

$$n_b(l) \propto l^{-D}, \tag{29}$$

where D is the fractal dimension of the nodal domain. The fractal dimension may then be extracted by a linear fit to a log–log plot. We use only a 60×60 section of the nodal domain. This ensures that the number of lattice points in each box is an integer, provided we choose l as a factor of 60.

As an example of the method, we now consider one eigenvector of the map (15) with parameters $N = 61$, $k_1 = 0.05$ and $k_2 = 0.01$ (a more statistical approach will follow). In figure 7, a log–log plot of $n_b(l)$ versus l is shown for the largest nodal domain. In this case the slope yields a fractal dimension of $D^{\text{fit}} = 1.8998$. This is close to the theoretical value of $D = 91/48 (= 1.8958\ldots)$, especially when one takes into consideration the fact that the data cover only a small range in l. In order to check that this is not a coincidence, we now consider ways of combining the data for all eigenvectors.

A cumulative plot of the fractal dimensions of the largest nodal domains is shown in figure 8. This shows, for a given value of D, the fraction $D_c(D)$ of eigenvectors such that $D^{\text{fit}} \leqslant D$, for a given set pair of perturbation parameters. In this case, one finds a mean fractal dimension of 1.8579 with a variance of 0.0099. The same calculation for eigenvalues of map (20) with $k_1 = k_2 = 0.01$ gives fractal dimension 1.85(10).

In figure 9, this distribution is shown for several values of the perturbation parameters. The average fractal dimension over all perturbation parameters and all eigenvalues is equal to $D^{\text{fit}}_{\text{av}} = 1.8571$, and the variance is 0.0101. Therefore, there is a statistical error of ± 1 in the first decimal place. The computed fractal dimension is within a standard deviation of its theoretically

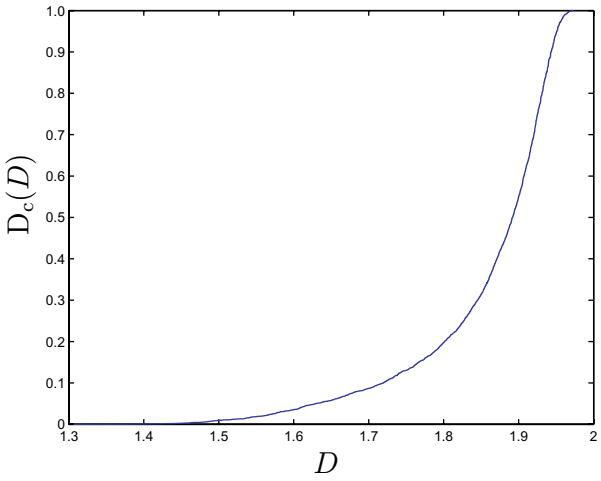

Figure 8. The cumulative fraction of eigenvectors $D_c(D)$ whose largest nodal domains have fractal dimension less than D for (15) with $N = 61$, $k_1 = 0.01$ and $k_2 = 0.02$. The mean fractal dimension for this set of parameters is $\bar{D} = 1.8579$ and its variance is $\mathrm{var}(D) = 0.0099$.

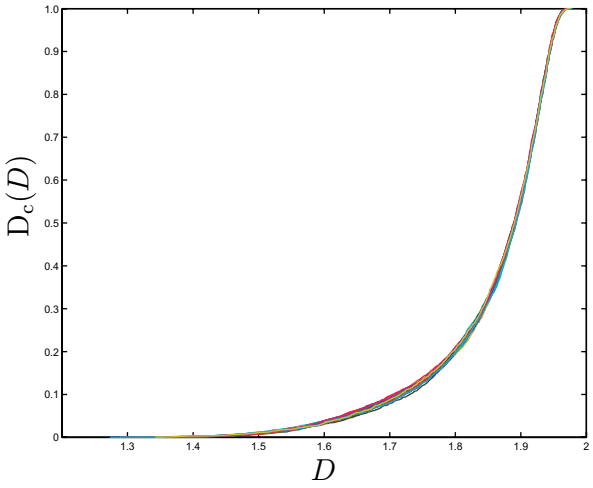

Figure 9. The cumulative fraction of eigenvectors $D_c(D)$ whose largest nodal domains have fractal dimension less than D for (15) with $N = 61$ and 20 different pairs of perturbation parameters k_1, $k_2 \in [0.01, 0.05]$. There is close agreement between the curves for different perturbation parameters

predicted value. For comparison, the simulations of uncorrelated percolation on a 61×61 lattice gave a mean fractal dimension of 1.8582 with variance 0.099. This shows that the difference between the computed fractal dimension and the theoretical value can be attributed to finite-size effects. As is seen in figure 9, the cumulative distributions of the fractal dimensions agree very closely for all values of the parameters.

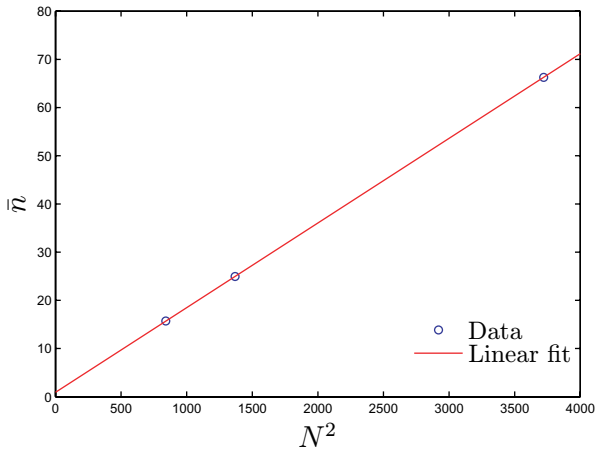

Figure 10. The mean number of nodal domains of unperturbed map (15) as a function of the number of sites, N^2. The straight line fit gives values for n_c and b.

3.4. The unperturbed cat map

The cat maps themselves do not conform to the random matrix expectations [14]. Instead, they are representative examples of arithmetic systems in which additional non-generic number theoretical symmetries lead to atypical eigenvalue and eigenvector statistics (see, for example [19]). (Indeed, in certain circumstances these symmetries can survive nonlinear perturbations [20].) An additional complication arises in that there are many values of N for which a nonvanishing proportion of the eigenvalues are exactly degenerate [10, 14, 21]. This leads to an ambiguity in the assignment of eigenfunctions. In this study, we restrict our attention to values of N which give non-degenerate eigenvalues.

The data for the unperturbed map given by (15) with $k_1 = k_2 = 0$ were also compared with the predictions (21)–(23) for the mean number of nodal domains. The data for the mean number of nodal domains are shown in figure 10. The linear fit gives the values

$$n_c^{\text{fit}} = 0.01757, \quad b^{\text{fit}} = 0.9102.$$

These values are in good agreement with the predictions in (22) and (23), so at this level the perturbed and unperturbed maps are similar. The supposed universality of b would then suggest that these two models lie in the same universality class, in spite of the presence of arithmetical symmetries. A similar analysis of the behaviour of $\text{var}(\nu)$ as a function of N gives the value $\alpha^{\text{fit}} = 0.3838N^2$, which is larger than the value in the perturbed case. For the map given by (20) analogous results are not available, because of a lack of values of N giving non-degenerate eigenvalues and hence a lack of points to extract the straight line fits.

One may also consider the area distribution of the nodal domains of the unperturbed map. As with the results for the perturbed cat maps, shown in section 3.2, one finds that the area distribution shows the expected power law behaviour. This is shown in figure 11. These results, and others to follow, indicate that the percolation model also applies to the cat maps themselves. It is worth emphasizing in this context that our justification of the percolation model only requires the joint eigenvector-component probability density (3) to be invariant under the sign flip $\Psi(\mathbf{Q}_i) \to -\Psi(\mathbf{Q}_i)$ for any single component $\mathbf{Q}_i \in \square_N$, independently of the signs of the

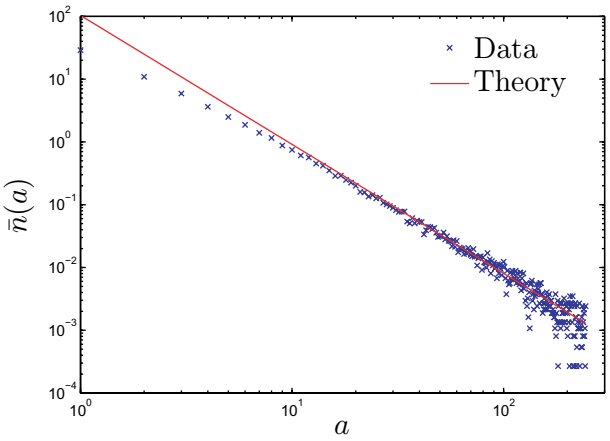

Figure 11. The calculated area distribution for the unperturbed map (15).

other components. This is much weaker than the full random-matrix assumption (from which it follows as a consequence), and may well still hold for the cat maps and other arithmetic quantum chaotic systems.

4. Conformal invariance and SLE

A recent development in two-dimensional critical systems is the application of conformal invariance. This allows the calculation of a number of interesting quantities, such as the crossing probability considered in [22]. This measures the probability that, for critical percolation in a given domain, there is a percolation cluster connecting two disjoint arcs on the domain boundary. Here, we test the crossing formula for the map eigenfunctions. In this case, we consider the probability that there is a nodal domain connecting a fixed section of length x at $Q_2 = 0$ to $Q_2 = N - 1$, as shown in figure 12.

The method applied in [22] is to find a conformal map which takes the domain to the upper half of the complex plane. The points on the boundary are then mapped to points z_j, $j = 1, \ldots, 4$ on the real line. This map is not unique, however, as the upper half-plane is invariant under the real Möbius transformations

$$z \to \frac{az+b}{cz+d}, \quad a, b, c, d, \in \mathbb{R}.$$

The crossing probability is then a function of the *cross ratio* η, an invariant under these transformations defined as

$$\eta = \frac{(z_2 - z_1)(z_4 - z_3)}{(z_3 - z_1)(z_4 - z_2)}. \tag{30}$$

The crossing formula is expressed in terms of the cross ratio as [22]

$$\pi((z_1, z_2), (z_3, z_4)) = \frac{3\Gamma(2/3)}{\Gamma(1/3)^2}\eta^{1/3}{}_2F_1(1/3, 2/3; 4/3; \eta), \tag{31}$$

where ${}_2F_1$ is a hypergeometric function [23, **15.1.1**].

In order to compare our results with this formula, we must decide how the boundaries of the domain are defined. We have previously been analysing the nodal domains on the torus,

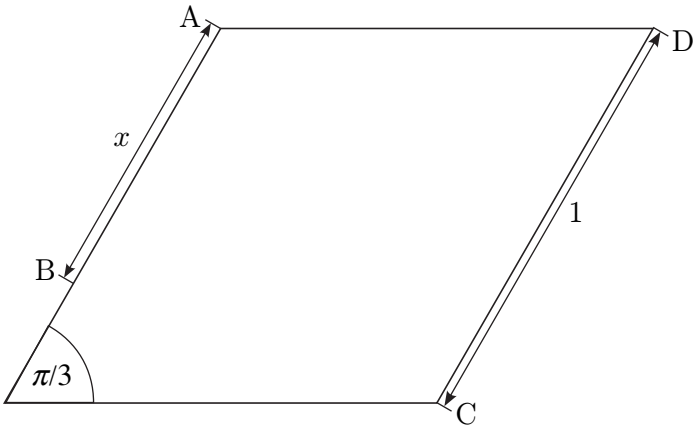

Figure 12. The geometry for evaluating the crossing probabilities π_h and π_{hv}. The crossing probability π_h is the probability of a nodal domain occurring which touches the boundaries of the parallelogram in the arcs AB and CD. The probability π_{hv} is the probability that a nodal domain touches the boundary in each of the arcs AB, BC, CD and DA. The parameter x varies between 0 and 2, with values $x > 1$ corresponding to when point B lies on the lower boundary.

while the crossing formula applies to domains with boundaries. We will therefore analyse the nodal domains in the absence of the periodicity requirement, and consider the domain as $0 \leqslant Q_i \leqslant N-1$ for $i = 1, 2$. This changes the assignment of the nodal domains.

Furthermore, we need to find a conformal transformation taking the resulting domain to the upper half-plane. Such a transformation is derived in [24], where it is found that a map taking $\mathbb{H}$ to the domain we consider is given by the Schwartz–Christoffel transformation

$$f(z) = \frac{\sqrt{3}}{2} \int_0^z t^{-1/3}(1-t)^{-2/3}(1-t/2)^{-1/3}\,\mathrm{d}t, \tag{32}$$

where the branch is chosen such that each of the factors t, $(1-t)$ and $(1-t/2)$ have argument π if they are real and negative. The map from the parallelogram to the upper half-plane is then given by f^{-1}. This transformation gives the cross ratio η in terms of x, and allows the measured frequency of crossings to be compared with the Cardy crossing formula (31).

The results for the crossing formula are shown in figure 13. The data were obtained by counting the number of eigenvectors of the map (15) containing a crossing of the type shown in figure 12, as a fraction of the total number of eigenvectors.

By making the assumption that we obtain the number of crossings of this type by making N^2 trials of a Bernoulli process with probability given by the Cardy crossing formula, it is possible to make error estimates and find whether the data lies within a given confidence interval of the predicted curve. The probability of there being a crossing in any particular realization is given by $\pi_h(\eta)$, and hence the probability of there being n realizations containing a crossing is given by the binomial distribution

$$p(n, N^2) = \binom{N^2}{n} \pi_h(\eta)^n (1-\pi_h(\eta))^{N^2-n}, \tag{33}$$

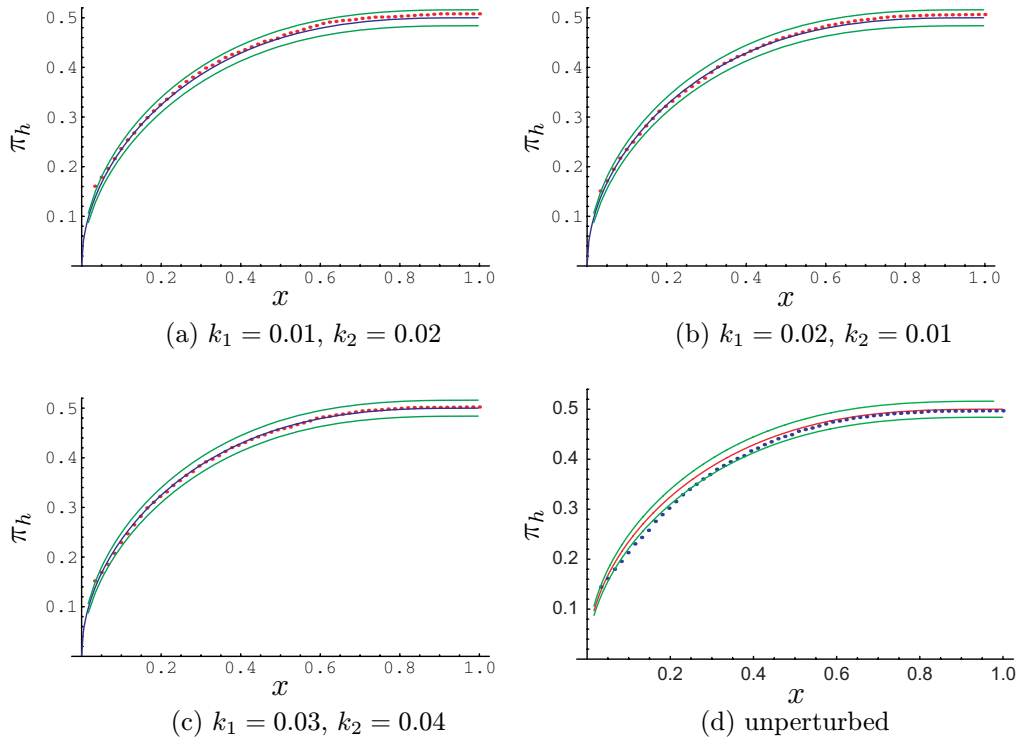

(a) $k_1 = 0.01$, $k_2 = 0.02$ (b) $k_1 = 0.02$, $k_2 = 0.01$

(c) $k_1 = 0.03$, $k_2 = 0.04$ (d) unperturbed

Figure 13. Numerics for the crossing formula for map (15) with $N = 61$ and varying perturbation parameters, compared with the crossing formula prediction. The green lines show the upper and lower confidence limits given by equation (35).

where $\binom{a}{b}$ is the binomial coefficient giving the number of combinations when choosing b objects out of a total of a possibilities. The binomial distribution tends to a Gaussian for large N^2. In this case, the distribution of $x = n/N^2$ is given asymptotically by

$$\mathcal{P}\{n/N^2 = x\} \sim \frac{N}{\sqrt{2\pi\pi_h(\eta)(1-\pi_h(\eta))}} \exp\left(-\frac{N^2(x-\pi_h(\eta))^2}{2\pi_h(\eta)(1-\pi_h(\eta))}\right). \tag{34}$$

This is used to put a 95% confidence interval on the measured value of x, which is

$$\pi_h(\eta) - 1.96\sigma_{\text{cross}} < x < \pi_h(\eta) + 1.96\sigma_{\text{cross}}, \tag{35}$$

where the standard deviation σ_{cross} for the distribution (34) is given by:

$$\sigma_{\text{cross}} = \frac{\sqrt{\pi_h(\eta)(1-\pi_h(\eta))}}{N}. \tag{36}$$

The data obtained for a particular realization of the map (15) are shown in figure 13, along with the errors obtained from formula (35). Any points lying outside these errors would indicate an error either in the assumed probability function or the assumption that the eigenvectors are independent. As seen in the figures, this only occurs for small x, where the effects of the underlying discrete lattice will be most apparent. This difference is attributable to finite size effects, as demonstrated in figure 14 for data obtained from Monte Carlo simulations of

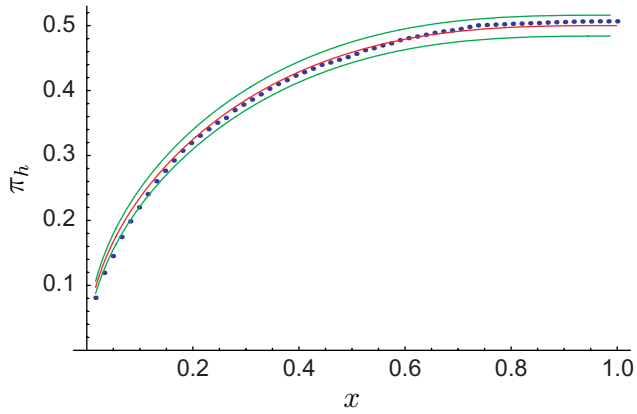

Figure 14. Number of crossings as a function of x from Monte Carlo simulations of percolation on a 61×61 lattice with comparison to Cardy crossing formula (31). This shows deviations from the Cardy crossing formula which lie outside the confidence interval at low values of x.

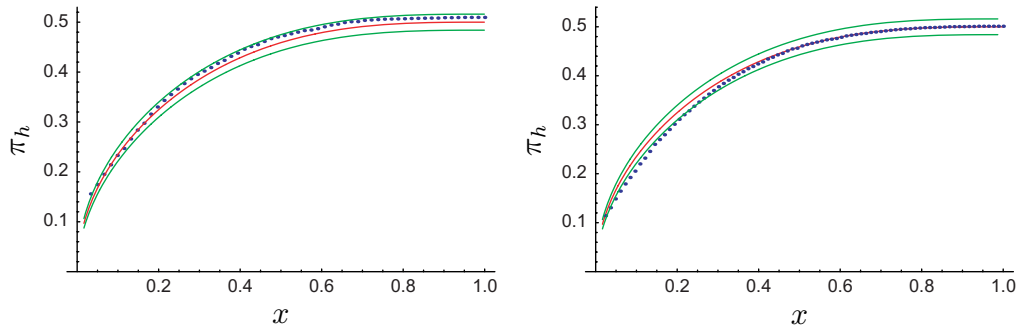

(a) $N = 61$, $k_1 = 0.01$, $k_2 = 0.01$ (b) $N = 83$, unperturbed

Figure 15. Numerics for the crossing formula for map (20), compared with the crossing formula prediction (31). The outer lines show the upper and lower confidence limits given by equation (35).

percolation on a 61×61 lattice. In this case we also find deviations from the Cardy crossing formula for small x. These calculations were also repeated for the map given in (20), and the results are shown in figure 15.

5. SLE calculations

Stochastic Loewner evolution or Schramm–Loewner evolution (SLE), introduced in [25], is a process for generating self-similar, non self-intersecting curves in two dimensions from a stochastic differential equation. We shall concentrate on the case of chordal SLE, which relates to curves in the upper half of the complex plane, henceforth referred to as $\mathbb{H}$.

We consider a curve γ growing from the origin in $\mathbb{H} \cup \{0\}$. The main idea of this method is that one can fully describe a given section of the curve by the conformal map $g : \mathbb{H} \setminus \gamma \to \mathbb{H}$. This conformal map is unique provided that it is required to satisfy the additional condition

$$\lim_{z \to \infty} (g(z) - z) = 0. \tag{37}$$

The Laurent expansion of such a map around $z = \infty$ is consequently required to have the form

$$g(z) = z + \sum_{i=1}^{\infty} \frac{a_i}{z^i}, \tag{38}$$

where the first term in this expansion, a_1, gives a measure of the 'size' of the domain which is removed by this map. By defining a 'time', t such that $a_1(\gamma([0, t])) = 2t$, the growth of the curve may be completely described by the following differential equation for the conformal map g_t:

$$\frac{\partial g_t(z)}{\partial t} = \frac{2}{g_t(z) - \xi_t}, \tag{39}$$

where the tip of the curve $\gamma([0, t])$ is mapped to $\xi_t \in \mathbb{R}$. This is the Loewner differential equation. One can substitute an arbitrary continuous function for ξ_t and the resulting conformal maps will describe the growth of a curve in $\mathbb{H}$.

The innovation of Schramm was to allow ξ_t to be a stochastic variable. Under the condition that the curves are conformally invariant and are statistically unchanged under reflection through $x = 0$, the only possibility for ξ_t is that it is proportional to a one-dimensional Brownian motion, i.e. $\xi_t = \sqrt{\kappa} B_t$. The conformal maps then satisfy the stochastic differential equation

$$\frac{\partial g_t(z)}{\partial t} = \frac{2}{g_t - \sqrt{\kappa} B_t}, \quad g_0(z) = z. \tag{40}$$

The curve is recovered from the map g_t using $\gamma(t) = \lim_{z \to \sqrt{\kappa} B_t} g_t^{-1}(z)$. This gives a family of conformally invariant curves generated by a process which is parameterized by κ, and is denoted SLE_κ.

It has been proven by Smirnov [26] that the boundaries of critical percolation clusters for site percolation on the triangular lattice are described by SLE_6. This should also be true of the boundaries of nodal domains of the quantum map eigenfunctions. We verify this numerically, following the methods of [27]. The process of extracting a putative SLE trace from an eigenfunction is shown in figure 16. A nodal line is defined as the boundary between hexagons with opposite signs. The trace follows a nodal line beginning in the column $Q_2 = 0$ until such a time as it returns to the column $Q_2 = 0$ or alternatively hits one of the other boundaries. In the first case, the boundary is followed until such a time as another nodal line is reached, which is then followed into the domain. In the second case, the process is terminated, and we have our complete trace.

In order to extract the forcing function from the trace, a modified version of the 'Zipper' algorithm introduced in [28] is used. This method is reliant on an explicit solution [29] of the Loewner equation with the driving function

$$\xi_t = 2[\varrho t]^{1/2}. \tag{41}$$

The map g_t which solves this equation is given implicitly by

$$H(g_t/t^{1/2}) = 2\ln(z/t^{1/2}), \tag{42}$$

where

$$H(G) := \frac{2y_+ \ln(G - y_-) - 2y_- \ln(G - y_+)}{y_+ - y_-} \tag{43}$$

with $y_\pm = \varrho^{1/2} \pm (\varrho + 4)^{1/2}$.

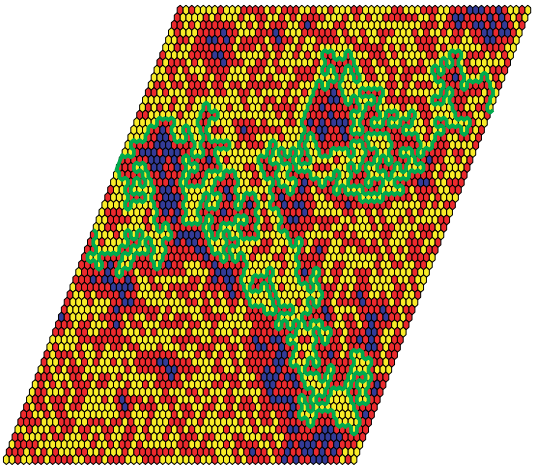

Figure 16. Computing the putative SLE trace from an eigenfunction of the quantum map. A nodal line beginning in the first column is followed until it again reaches this column. The boundary is then followed until another nodal line is reached, and the process continues as before.

The tip of the growing curve at time t is given by the point at which $g_t(\gamma(t)) = \xi_t$. Hence, the curve $\gamma(t)$ defined by equation (42) is given by [29]

$$\gamma(t) = Bt^{1/2}, \tag{44}$$

where the coefficient is given by

$$B = 2\left(\frac{(\varrho+4)^{1/2}+\varrho^{1/2}}{(\varrho+4)^{1/2}-\varrho^{1/2}}\right)^{(1/2)(\varrho^{1/2}/(\varrho+4)^{1/2})} \exp\left[\frac{1}{2}\pi i\left(1-\frac{\varrho^{1/2}}{(\varrho+4)^{1/2}}\right)\right]. \tag{45}$$

The trace corresponding to the driving function (41) is a straight line starting from the origin at an angle

$$\theta = \frac{\pi}{2}\left(1-\frac{\varrho^{1/2}}{(\varrho+4)^{1/2}}\right)$$

to the real axis. Using this formula, it is straightforward to obtain the parameters ϱ and t which give a conformal map to absorb a given straight line growing from the boundary. This is shown in figure 17. The main computational difficulty then lies in inverting (42) in order to find the mapping of the remaining points. This is achieved using Newton's method, as described in [28, section 4].

The result of the calculations is a series of times and values of ϱ for each straight line section as it is absorbed. These may then be used to obtain a value of the forcing function at any time until the process is stopped. In order to study the statistics of the forcing function, we may only consider times up to the first time any of the traces reaches the boundary. It is important to note that this approach is only valid in the case where the trace corresponds to SLE_6, as this has the important *locality* property (see, for example [30]). This means that the distribution of its trace in a domain with a boundary is identical to that in the half-plane until the trace touches the boundary. If this property did not hold, we would have to consider instead an SLE process confined to the parallelogram. The property of locality is unique to SLE_6.

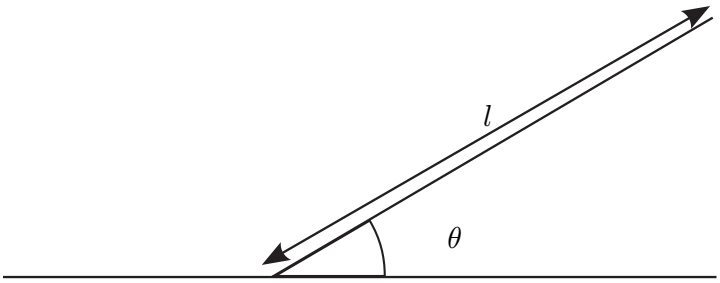

Figure 17. The line of singularities for maps derived from the Loewner differential equation with the forcing given by (41).

In order to extract the value of κ from the map eigenfunctions, the forcing function was calculated for traces taken from each of the eigenfunctions. The statistics of the forcing function then gives a test of the applicability of the SLE description. The most important statistics are those for the mean and variance of ξ_t. According to the SLE description, these should be given by

$$\langle \xi_t \rangle = 0, \quad \langle \xi_t^2 \rangle = \kappa t. \tag{46}$$

In figure 18, the data for $\langle \xi_t^2 \rangle$ are plotted as a function of $\sqrt{t}$ for map (15) with $k_1 = 0.02$, $k_2 = 0.01$. Also shown in this plot are data from Monte Carlo simulations of percolation. In the time range where both the cat map eigenfunction data and the Monte Carlo simulation data are available, the variances of the driving functions can be seen to be in close agreement. However, the best fit to the data from the cat map eigenfunctions is unstable, and we instead make a fit to the percolation data. This results in the dependence $\langle \xi_t^2 \rangle = 5.9t + 6.4\sqrt{t}$, giving a value of $\kappa = 5.9$. This shows that the behaviour of the forcing function is consistent with the expectation that it is given by SLE_6. We note that this type of fit gives a significantly more stable and accurate result for κ than that originally used in [9]. For another refinement that also improves the fitting process, see [31]. The data for the quantum map (20) is shown in figure 19. The fit to this data gives $\langle \xi_t^2 \rangle = 6.4t + 1.4\sqrt{t} - 1.3$, again in agreement with the conjectured SLE_6 behaviour.

We have also repeated these numerical experiments for the (unperturbed) quantum cat maps. The data for the unperturbed map (20) are shown in figure 20, and in this case we find that a fit to the data gives $\langle \xi_t^2 \rangle = 5.8t + 2.7\sqrt{t} - 1.5$, again supporting the conjectured SLE_6 model for the statistical properties of the nodal lines. It would be most interesting if this could be proved using the arithmetical techniques available in this case (see, for example [19]).

Appendix. Quantization of torus maps

In this appendix, the quantization procedure used to obtain the quantized map (15) will be explained. First, the quantization of linear hyperbolic maps of the plane will be derived. The restriction of these quantum maps to the torus will then be computed and from this we will find the higher dimensional analogues of the quantized cat maps.

The cat maps are chaotic, linear maps of the torus $\mathbb{T}^{2L}$, and may be written in the following form:

$$M : \begin{pmatrix} \mathbf{q} \\ \mathbf{p} \end{pmatrix} \to \begin{pmatrix} A & B \\ C & D \end{pmatrix} \begin{pmatrix} \mathbf{q} \\ \mathbf{p} \end{pmatrix} \qquad \text{mod } 1, \tag{A.1}$$

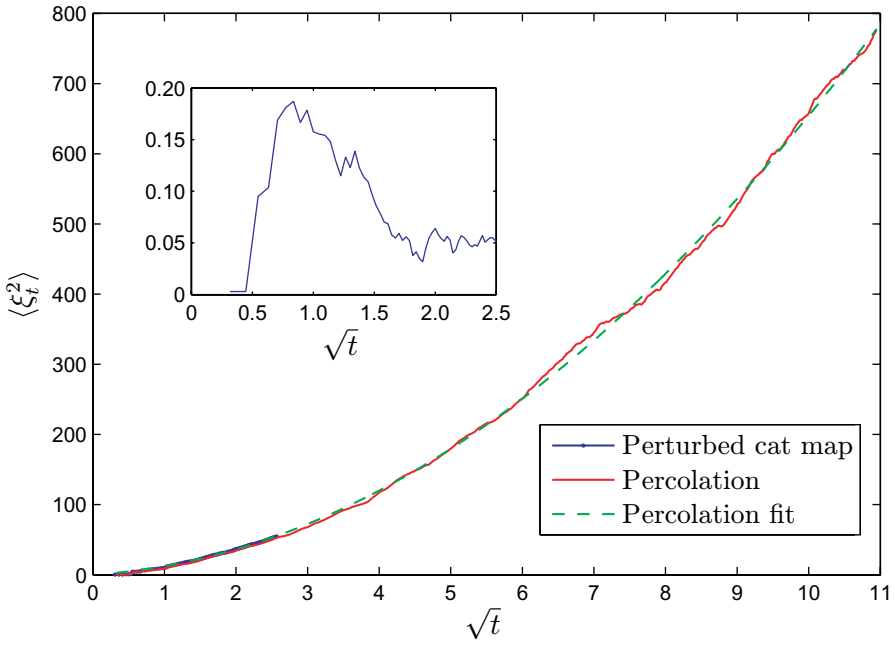

Figure 18. The variance of the forcing function for eigenfunctions of the quantum map (15) with $k_1 = 0.02$ and $k_2 = 0.01$. Also shown is the variance of the forcing function for Monte Carlo simulations of percolation with a fit of the form $\xi_t = \kappa_m t + ct^{1/2}$. The least-squares fit gives the values $\kappa_m = 5.9$ and $c = 6.4$. The inset figure shows the difference between the driving function of the perturbed cat map and the percolation simulation, expressed as a fraction of the perturbed cat map driving function. Note that the perturbed cat map data terminate at $\sqrt{t} \simeq 2.5$ in the main plot.

where A, B, C and D are integer $L \times L$ matrices and $\mathbf{q}$, $\mathbf{p}$ are L dimensional vectors. The condition that M is an integer matrix derives from the requirement that two points which are equivalent under translation by an integer vector should transform identically under the action of M. The requirement that the map is symplectic gives the following conditions:

$$AD^t - BC^t = I, \tag{A.2}$$

$$CD^t = DC^t, \tag{A.3}$$

$$C^t A = A^t C. \tag{A.4}$$

As discussed in the text, the eigenvectors of the quantized map should be periodic up to a phase factor. For simplicity, the phase factors are chosen to be zero in this case, giving

$$\psi(\mathbf{q} + \mathbf{e}_i) = \psi(\mathbf{q}), \tag{A.5}$$

$$\tilde{\psi}(\mathbf{p} + \mathbf{e}_i) = \tilde{\psi}(\mathbf{p}), \tag{A.6}$$

where $\mathbf{e}_i$ are unit vectors in each of the basis directions. (For quantization with other choices of the phases, see [32].)

A constructive method for finding the quantization of the classical map was also proposed in [13]. The method used is a Weyl quantization based on the centre and chord representations

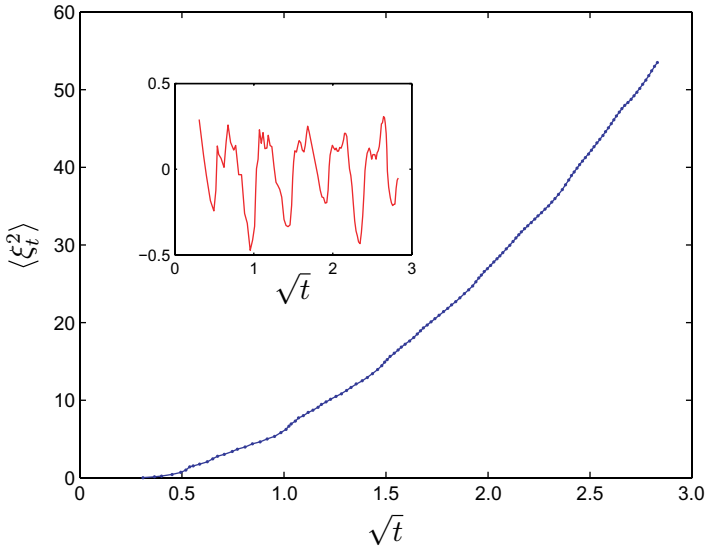

Figure 19. Behaviour of the SLE forcing function for map (20) with $N = 83$ and $k_1 = k_2 = 0.01$. The inset shows the difference between the measured variance and the fit given by $\langle \xi_t^2 \rangle = 6.4t + 1.4\sqrt{t} - 1.3$.

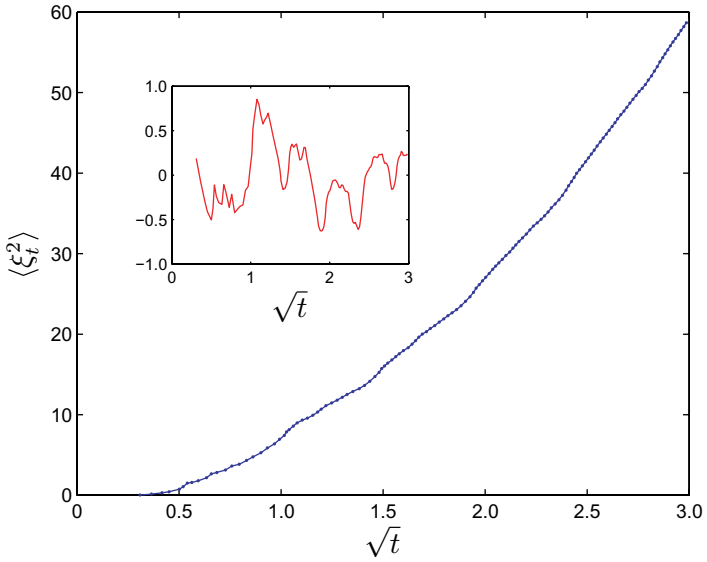

Figure 20. Forcing for unperturbed map (20) with $N = 83$. The inset shows the difference between the measured variance and the fit given by $\langle \xi_t^2 \rangle = 5.8t + 2.7\sqrt{t} - 1.5$.

of the classical maps. Quantization conditions for multidimensional cat maps were also derived in [13]. In this work, we will prefer an alternative method of quantization which is an extension of the Hannay–Berry method [10] to higher dimensions. This has the advantage that it works directly with the phase space representation of the map.

A.1. Quantization on the plane

In the case where C is a nonsingular matrix, the map M may be decomposed as follows:

$$\begin{pmatrix} A & B \\ C & D \end{pmatrix} = \begin{pmatrix} I & AC^{-1} \\ 0 & I \end{pmatrix} \begin{pmatrix} 0 & -I \\ I & 0 \end{pmatrix} \begin{pmatrix} I & DC^t \\ 0 & I \end{pmatrix} \begin{pmatrix} C & 0 \\ 0 & (C^t)^{-1} \end{pmatrix}. \tag{A.7}$$

Each of the matrices in this decomposition may be quantized on the plane by finding the Hamiltonian which generates the flow, and then solving the corresponding Weyl-ordered Schrödinger equation. There are three types of matrix in the decomposition (A.7):

$$M_1 = \begin{pmatrix} I & X \\ 0 & I \end{pmatrix}, \quad M_2 = \begin{pmatrix} 0 & -I \\ I & 0 \end{pmatrix}, \quad M_3 = \begin{pmatrix} Y & 0 \\ 0 & (Y^t)^{-1} \end{pmatrix}. \tag{A.8}$$

The propagator for matrices of type M_1 may be found by considering the time evolution given by the equations

$$\begin{pmatrix} \mathbf{q} \\ \mathbf{p} \end{pmatrix} \to \begin{pmatrix} I & Xt \\ 0 & I \end{pmatrix} \begin{pmatrix} \mathbf{q} \\ \mathbf{p} \end{pmatrix}, \tag{A.9}$$

where X is a symmetric matrix due to the requirement that M_1 is symplectic. This time evolution can be generated from Hamilton's equations using the Hamiltonian

$$H_1 = \tfrac{1}{2}\mathbf{p} \cdot X \cdot \mathbf{p}. \tag{A.10}$$

The quantization of the map M_1 may then be obtained as the quantum propagator of a system with Hamiltonian H_1 for $t = 1$. The propagator is given by

$$\begin{aligned} \hat{U}_{M_1} &= \exp\left(-\frac{\mathrm{i}\hat{H}_1}{\hbar}\right), \\ &= \exp\left(-\frac{\mathrm{i}\hat{\mathbf{p}} \cdot X \cdot \hat{\mathbf{p}}}{\hbar}\right). \end{aligned} \tag{A.11}$$

In the momentum representation, this may be written as

$$\langle \mathbf{p}' | \hat{U}_{M_1} | \mathbf{p} \rangle = \delta(\mathbf{p} - \mathbf{p}') \exp\left(-\frac{\mathrm{i}\mathbf{p} \cdot X \cdot \mathbf{p}}{\hbar}\right). \tag{A.12}$$

The propagator in the position representation is obtained by inserting the identity

$$\langle \mathbf{q} | \mathbf{p} \rangle = (2\pi\hbar)^{-L/2} \exp\left(\frac{\mathrm{i}\mathbf{q} \cdot \mathbf{p}}{\hbar}\right), \tag{A.13}$$

and integrating to obtain

$$\begin{aligned} \langle \mathbf{q}' | \hat{U}_{M_1} | \mathbf{q} \rangle &= \int\int \langle \mathbf{q}' | \mathbf{p}' \rangle \langle \mathbf{p}' | \hat{U}_{M_1} | \mathbf{p} \rangle \langle \mathbf{p} | \mathbf{q} \rangle \mathrm{d}^L\mathbf{p}\, \mathrm{d}^L\mathbf{p}', \\ &= \frac{1}{(2\pi\hbar)^L} \int\int \mathrm{e}^{(\mathrm{i}\mathbf{p}' \cdot \mathbf{q}'/\hbar)} \delta(\mathbf{p} - \mathbf{p}')\, \mathrm{e}^{-\frac{\mathrm{i}\mathbf{p} \cdot X \cdot \mathbf{p}}{\hbar}}\, \mathrm{e}^{-\frac{\mathrm{i}\mathbf{p} \cdot \mathbf{q}}{\hbar}} \mathrm{d}^L\mathbf{p}\, \mathrm{d}^L\mathbf{p}', \\ &= \frac{1}{(2\pi\hbar)^L} \int \exp\left[\frac{\mathrm{i}}{\hbar}\left(\mathbf{p} \cdot (\mathbf{q}' - \mathbf{q}) - \mathbf{p} \cdot X \cdot \mathbf{p}\right)\right] \mathrm{d}^L\mathbf{p}, \end{aligned} \tag{A.14}$$

where use has been made of equation (A.13). The remaining integral is a Gaussian integral which may be evaluated to give

$$\langle \mathbf{q}' | \hat{U}_{M_1} | \mathbf{q} \rangle = \frac{1}{(2\pi\hbar\mathrm{i})^{L/2}\sqrt{\det X}} \exp\left(\frac{\mathrm{i}}{2\hbar}(\mathbf{q} - \mathbf{q}') \cdot X^{-1} \cdot (\mathbf{q} - \mathbf{q}')\right). \tag{A.15}$$

The map M_2 may be considered as the $t = 3\pi/4$ case of the time evolution given by

$$\begin{pmatrix} \mathbf{q} \\ \mathbf{p} \end{pmatrix} \to \begin{pmatrix} I\cos t & I\sin t \\ -I\sin t & I\cos t \end{pmatrix} \begin{pmatrix} \mathbf{q} \\ \mathbf{p} \end{pmatrix}. \tag{A.16}$$

This time evolution may be derived from the Hamiltonian

$$H_2 = \frac{\mathbf{p}^2 + \mathbf{q}^2}{2}, \tag{A.17}$$

which is the Hamiltonian for a multidimensional harmonic oscillator. The propagator for the one-dimensional harmonic oscillator is given, for example in [33], by

$$\langle q'|\hat{U}|q\rangle = \frac{1}{\sqrt{2\pi\hbar}} \exp\left(-\frac{\mathrm{i}\pi\sigma_t}{4}\right) |\sin t|^{-1/2} \exp\left(\mathrm{i}\frac{(q^2+q'^2)\cos t - 2qq'}{2\hbar\sin t}\right), \tag{A.18}$$

where $\sigma_t = 2\nu + 1$ for $\nu\pi < t < (\nu+1)\pi$. The matrix M_2 does not mix different components of the position and momentum, so the propagator for the L dimensional system is simply the product of several one-dimensional propagators:

$$\langle \mathbf{q}'|\mathrm{e}^{-\mathrm{i}H_2 t/\hbar}|\mathbf{q}\rangle = \frac{1}{(2\pi\hbar)^{L/2}} \exp\left(-\frac{\mathrm{i}\pi L\sigma_t}{4}\right) |\sin t|^{-L/2} \exp\left(\mathrm{i}\frac{(\mathbf{q}^2+\mathbf{q}'^2)\cos t - 2\mathbf{q}\cdot\mathbf{q}'}{2\hbar\sin t}\right). \tag{A.19}$$

Setting $t = 3\pi/4$ in this expression gives

$$\langle \mathbf{q}'|\hat{U}_{M_2}|\mathbf{q}\rangle = \frac{1}{(2\pi\hbar)^{L/2}} \exp\left(\frac{\mathrm{i}\mathbf{q}\cdot\mathbf{q}'}{\hbar} - \frac{3\pi\mathrm{i}L}{4}\right). \tag{A.20}$$

Finally, the propagator for matrices of type M_3 may be considered as the $t = 1$ quantum propagator for classical motion given by

$$\begin{pmatrix} \mathbf{q} \\ \mathbf{p} \end{pmatrix} \to \begin{pmatrix} \mathrm{e}^{Zt} & 0 \\ 0 & \mathrm{e}^{-Z^t t} \end{pmatrix} \begin{pmatrix} \mathbf{q} \\ \mathbf{p} \end{pmatrix}, \tag{A.21}$$

where Z is a matrix defined such that $\mathrm{e}^Z = Y$. The Hamiltonian which generates this classical motion is given by

$$H_3 = \mathbf{p}\cdot Z\cdot\mathbf{q}, \tag{A.22}$$

which leads to a Weyl-ordered Hamiltonian given by

$$\hat{H}_3 = \hat{\mathbf{q}}\cdot Z^t\cdot\hat{\mathbf{p}} - \frac{\mathrm{i}\hbar\,\mathrm{Tr}\,Z}{2}. \tag{A.23}$$

The wavefunction may then be found by solving the time-dependent Schrödinger equation derived from this Hamiltonian, given by

$$\left(\mathbf{q}\cdot Z^t\cdot\frac{\partial}{\partial\mathbf{q}} + \frac{\mathrm{Tr}\,Z}{2} + \frac{\partial}{\partial t}\right)\psi(\mathbf{q},t) = 0. \tag{A.24}$$

Define a matrix S containing the right eigenvectors of Z^t such that $S^{-1}Z^tS = V$ where V is a diagonal matrix containing the eigenvalues of Z^t. By making the coordinate transformation $\mathbf{r} = S^t\mathbf{q}$ in (A.24) one may obtain

$$\left(\mathbf{r}\cdot V\cdot\frac{\partial}{\partial\mathbf{r}} + \frac{\mathrm{Tr}\,Z}{2} + \frac{\partial}{\partial t}\right)\psi'(\mathbf{r},t) = 0, \tag{A.25}$$

$$\left(\sum_{i=1}^{L}\frac{\partial}{\partial s_i}+\frac{\operatorname{Tr} Z}{2}+\frac{\partial}{\partial t}\right)\chi(\mathbf{s},t)=0, \tag{A.26}$$

where the second equation is obtained by a coordinate transformation $\mathbf{r}=\exp(V\mathbf{s})$. Now define an orthogonal matrix R such that the top row is given by

$$R_{1,i}=\frac{1}{\sqrt{N}}, \tag{A.27}$$

and make a further coordinate transformation $\mathbf{x}=R\mathbf{s}/\sqrt{N}$ to obtain the equation

$$\left(\frac{\partial}{\partial x_1}+\frac{\partial}{\partial t}+\frac{\operatorname{Tr} Z}{2}\right)F(\mathbf{x},t)=0. \tag{A.28}$$

This has the solution

$$F(\mathbf{x},t)=G(x_1-t,x_2,\ldots,x_L)\exp\left(-\frac{\operatorname{Tr} Z(x_1+t)}{4}\right). \tag{A.29}$$

By solving this equation with the initial condition $\psi(\mathbf{q},0)=\Phi(\mathbf{q})$, and substituting back for $\mathbf{x}$ in terms of $\mathbf{q}$ we obtain the solution

$$\psi(\mathbf{q},t)=\exp\left(-\frac{\operatorname{Tr} Zt}{2}\right)\Phi(Y^{-1}\mathbf{q}). \tag{A.30}$$

This means that the quantum propagator, in the position representation, may be written as

$$\langle\mathbf{q}'|U_{M_3}|\mathbf{q}\rangle=\frac{1}{\sqrt{\det Y}}\delta(\mathbf{q}-Y^{-1}\mathbf{q}'). \tag{A.31}$$

A unitary map corresponding to the composition of two classical maps is given, up to a constant phase, by the product of their corresponding quantum maps. By using the decomposition (A.7) and inserting the identity operator $\int|\mathbf{q}\rangle\langle\mathbf{q}|\mathrm{d}\mathbf{q}$ three times, we obtain the following formula for the quantized map on the plane, under the assumption that the matrices A, B, C and D are non-singular:

$$\begin{aligned}\langle\mathbf{q}_2|U|\mathbf{q}_1\rangle=&\int\int\int\frac{(\mathrm{i}h)^{-L/2}}{\sqrt{\det(AC^{-1})}}\exp\left[\frac{\mathrm{i}}{2\hbar}\left((\mathbf{x}_1-\mathbf{q}_2)\cdot CA^{-1}\cdot(\mathbf{x}_1-\mathbf{q}_2)\right)\right]\\&\times\frac{1}{h^{L/2}}\exp\left(\frac{\mathrm{i}\mathbf{x}_1\cdot\mathbf{x}_2}{\hbar}-\frac{3\pi\mathrm{i}L}{4}\right)\frac{(\mathrm{i}h)^{-L/2}}{\sqrt{\det(DC^t)}}\\&\times\exp\left[\frac{\mathrm{i}}{2\hbar}(\mathbf{x}_3-\mathbf{x}_2)\cdot(C^t)^{-1}D^{-1}\cdot(\mathbf{x}_3-\mathbf{x}_2)\right]\frac{\delta(\mathbf{q}_1-C^{-1}\mathbf{x}_3)}{\sqrt{\det C}}\,\mathrm{d}\mathbf{x}_3\,\mathrm{d}\mathbf{x}_2\,\mathrm{d}\mathbf{x}_1.\end{aligned} \tag{A.32}$$

The integral over $\mathbf{x}_3$ may be performed using the properties of the Dirac delta function. First, we choose a basis in $\mathbf{x}_3$ which consists of the eigenvectors of C. Then use the fact that $\delta(ax)=\delta(x)/|a|$, where a is a constant. The integral over $\mathbf{x}_3$ gives

$$\begin{aligned}\langle\mathbf{q}_2|U|\mathbf{q}_1\rangle=&\sqrt{\frac{\det C}{\det(AD)}}\left(\frac{1}{\mathrm{i}h^3}\right)^{L/2}\int\int\exp\left[\frac{\mathrm{i}}{2\hbar}\left((\mathbf{x}_1-\mathbf{q}_2)\cdot CA^{-1}\cdot(\mathbf{x}_1-\mathbf{q}_2)\right)\right]\\&\times\exp\left[\frac{\mathrm{i}}{2\hbar}\left(2\mathbf{x}_1\cdot\mathbf{x}_2+(C\mathbf{q}_1-\mathbf{x}_2)\cdot(C^t)^{-1}D^{-1}\cdot(C\mathbf{q}_1-\mathbf{x}_2)\right)\right]\mathrm{d}\mathbf{x}_2\,\mathrm{d}\mathbf{x}_1.\end{aligned} \tag{A.33}$$

The substitutions $\mathbf{y}_1 = \mathbf{x}_1 - \mathbf{q}_2$ and $\mathbf{y}_2 = \mathbf{x}_2 - C\mathbf{q}_1$ in (A.33) give an equation which, after completing the square and using the symplectic condition (A.4) in the form $(C^t)^{-1}A^t = AC^{-1}$, may be written as

$$\langle \mathbf{q}_2|U|\mathbf{q}_1\rangle = \sqrt{\frac{\det C}{\det(AD)}}\left(\frac{1}{\mathrm{i}h^3}\right)^{L/2}\int\int \exp\left[-\frac{\mathrm{i}}{2\hbar}(\mathbf{y}_2+C\mathbf{q}_1)\cdot AC^{-1}\cdot(\mathbf{y}_2+C\mathbf{q}_1)\right]$$
$$\times\exp\left[\frac{\mathrm{i}}{2\hbar}(\mathbf{y}_1+AC^{-1}(\mathbf{y}_2+C\mathbf{q}_1))\cdot CA^{-1}\cdot(\mathbf{y}_1+AC^{-1}(\mathbf{y}_2+C\mathbf{q}_1))\right]$$
$$\times\exp\left[\frac{\mathrm{i}}{2\hbar}\mathbf{y}_2\cdot(C^t)^{-1}D^{-1}\cdot\mathbf{y}_2+2\mathbf{q}_2\cdot(\mathbf{y}_2+C\mathbf{q}_1)\right]\mathrm{d}\mathbf{y}_2\,\mathrm{d}\mathbf{y}_1. \tag{A.34}$$

Performing the Gaussian integration over $\mathbf{y}_1$ in this formula gives

$$\langle \mathbf{q}_2|U|\mathbf{q}_1\rangle = \frac{1}{\det D}\left(\frac{1}{h}\right)^L\exp\left(\frac{\mathrm{i}}{2\hbar}(2\mathbf{q}_2\cdot C\cdot\mathbf{q}_1-\mathbf{q}_1\cdot C^tA\cdot\mathbf{q}_1)\right)\int\mathrm{d}\mathbf{y}_2$$
$$\times\exp\left[\frac{\mathrm{i}}{2\hbar}\left(\mathbf{y}_2\cdot[(C^t)^{-1}D^{-1}-AC^{-1}]\mathbf{y}_2-2\mathbf{y}_2\cdot A\cdot\mathbf{q}_1+2\mathbf{q}_2\cdot\mathbf{y}_2\right)\right]. \tag{A.35}$$

Using the symplectic conditions again, it can be shown that $(C^t)^{-1}D^{-1}-AC^{-1} = -BD^{-1}$. By using this in (A.35) and completing the square, we obtain

$$\langle \mathbf{q}_2|U|\mathbf{q}_1\rangle = \frac{1}{\det D}\left(\frac{1}{h}\right)^L\exp\left[\frac{\mathrm{i}}{2\hbar}(2\mathbf{q}_2\cdot C\mathbf{q}_1-\mathbf{q}_1\cdot C^tA\cdot\mathbf{q}_1+(A\mathbf{q}_1-\mathbf{q}_2)\cdot DB^{-1}\cdot(A\mathbf{q}_1-\mathbf{q}_2))\right]$$
$$\times\int\exp\left[-\frac{\mathrm{i}}{2\hbar}(\mathbf{y}_2+A\mathbf{q}_1-\mathbf{q}_2)\cdot BD^{-1}\cdot(\mathbf{y}_2+A\mathbf{q}_1-\mathbf{q}_2)\right]\mathrm{d}\mathbf{y}_2. \tag{A.36}$$

Integration over $\mathbf{y}_2$ and the identity $A^tDB^{-1}A-C^tA = B^{-1}A$, which again follows from the symplectic conditions, lead to our final expression for the propagator

$$\langle \mathbf{q}_2|U|\mathbf{q}_1\rangle = \frac{\mathrm{i}^{L/2}}{\sqrt{h^L\det B}}\exp\left[\frac{\mathrm{i}}{2\hbar}(\mathbf{q}_2\cdot DB^{-1}\cdot\mathbf{q}_2+\mathbf{q}_1\cdot B^{-1}A\cdot\mathbf{q}_1-2\mathbf{q}_2\cdot(B^t)^{-1}\cdot\mathbf{q}_1)\right]. \tag{A.37}$$

This propagator is valid for all linear, hyperbolic maps on the plane with nonsingular A, B, C and D.

A.2. Quantization on the torus

Now consider the quantum equivalent of a classical map on the $2L$-dimensional torus.

$$\begin{pmatrix}\mathbf{q}_{n+1}\\ \mathbf{p}_{n+1}\end{pmatrix} = \begin{pmatrix}A & B\\ C & D\end{pmatrix}\begin{pmatrix}\mathbf{q}_n\\ \mathbf{p}_n\end{pmatrix} \quad \mathrm{mod}\ 1. \tag{A.38}$$

As discussed in section 2, the periodicity of the phase space restricts the wavefunctions to be supported on a discrete set of points in both position and momentum. The action of the plane propagator (A.37) on a wavefunction is given by

$$\psi(\mathbf{q}_2) = \int\langle \mathbf{q}_2|U|\mathbf{q}_1\rangle\psi(\mathbf{q}_1)\,\mathrm{d}\mathbf{q}_1, \tag{A.39}$$

Taking an eigenfunction of the form (1), we find that the quantum map takes $\psi(\mathbf{q}_1)$ to $\psi(\mathbf{q}_2)$, given by

$$\psi(\mathbf{q}_2) = \frac{(\mathrm{i}N)^{L/2}}{\sqrt{\det B}} \exp\left[\mathrm{i}\pi N \mathbf{q}_2 \cdot DB^{-1} \cdot \mathbf{q}_2\right] \sum_{\mathbf{Q}_1 \in \square_N} \Psi(\mathbf{Q}_1) \times \exp\left[\frac{\mathrm{i}\pi}{N}(\mathbf{Q}_1 \cdot B^{-1}A \cdot \mathbf{Q}_1 - 2N\mathbf{q}_2 \cdot (B^t)^{-1} \cdot \mathbf{Q}_1)\right] h_N(\mathbf{q}_2, \mathbf{Q}_1), \tag{A.40}$$

where

$$h_N(\mathbf{q}_2, \mathbf{Q}_1) = \sum_{\mathbf{l} \in \mathbb{Z}^L} \exp\left[\mathrm{i}\pi N \left(\mathbf{l} \cdot A^t (B^t)^{-1} \cdot \mathbf{l} + 2\left(\frac{A\mathbf{Q}_1}{N} - \mathbf{q}_2\right) \cdot (B^t)^{-1} \cdot \mathbf{l}\right)\right]. \tag{A.41}$$

This sum may be evaluated by writing $\mathbf{l} = \mathbf{m} + 2B^t\mathbf{n}$, where $\mathbf{m}$ is an integer point in the transformation of the unit cell, $\square$, by the matrix $2B^t$, and $\mathbf{n} \in Z^L$. This gives

$$h_N(\mathbf{q}_2, \mathbf{Q}_1) = \sum_{\mathbf{m} \in 2B^t\square} \exp\left[\mathrm{i}\pi N \left(\mathbf{m} \cdot A^t (B^t)^{-1} \cdot \mathbf{m} + 2\left(\frac{A\mathbf{Q}_1}{N} - \mathbf{q}_2\right) \cdot (B^t)^{-1} \cdot \mathbf{m}\right)\right] \times \sum_{\mathbf{n} \in Z^L} \exp\left[\mathrm{i}\pi N \left(4\mathbf{m} \cdot A^t \cdot \mathbf{n} + 4\mathbf{n} \cdot BA^t \cdot \mathbf{n} + 4\left(\frac{A\mathbf{Q}_1}{N} - \mathbf{q}_2\right) \cdot \mathbf{n}\right)\right]. \tag{A.42}$$

The second sum can be evaluated using the Poisson summation formula,

$$\sum_{\mathbf{l} \in Z^L} f(\mathbf{l}) = \sum_{\mathbf{l}' \in Z^L} \int_{\mathbf{x} \in R^L} f(\mathbf{x}) \exp(2\pi \mathrm{i}\mathbf{l}' \cdot \mathbf{x})\, \mathrm{d}^L\mathbf{x}. \tag{A.43}$$

We observe that in (A.42) the majority of the terms are integer multiples of 2π. Hence the sum over $\mathbf{n}$ becomes

$$\begin{aligned} \sum_{\mathbf{n} \in \mathbb{Z}^L} \exp\left(-4\pi \mathrm{i}N\mathbf{n} \cdot \mathbf{q}_2\right) &= \sum_{\mathbf{n}' \in Z^L} \int_{\mathbf{x} \in R^L} \exp\left(2\pi \mathrm{i}\mathbf{x} \cdot \mathbf{n}' - 4\pi \mathrm{i}N\mathbf{x} \cdot \mathbf{q}_2\right) \mathrm{d}^L\mathbf{x}, \\ &= \sum_{n' \in Z^L} \delta^L\left(\mathbf{n}' - 2N\mathbf{q}_2\right), \\ &= \frac{1}{(2N)^L} \sum_{\mathbf{n}' \in Z^L} \delta^L\left(\mathbf{q}_2 - \frac{\mathbf{n}'}{2N}\right), \end{aligned} \tag{A.44}$$

where (A.43) has been utilized in the second line. Consequently, each component of $\mathbf{q}_2$ is restricted to be a half-integer multiple of $1/N$.

The function h_N may now be rewritten as

$$h_N(\mathbf{q}_2, \mathbf{Q}_1) = \frac{1}{(2N)^L} \sum_{\mathbf{n}' \in Z^L} \sum_{\mathbf{m} \in 2B^t\square} \exp\left(\mathrm{i}\Phi(\mathbf{m})\right) \delta^L\left(\mathbf{q}_2 - \frac{\mathbf{n}'}{2N}\right), \tag{A.45}$$

where

$$\Phi(\mathbf{m}) := N\pi \left(\mathbf{m} \cdot A^t (B^t)^{-1} \cdot \mathbf{m} + 2\left(\frac{A\mathbf{Q}_1}{N} - \frac{\mathbf{n}'}{2N}\right) \cdot (B^t)^{-1} \cdot \mathbf{m}\right). \tag{A.46}$$

Consider the change in the phase $\Phi(\mathbf{m})$ when $\mathbf{m}$ is shifted by $B^t\mathbf{e}_j$, where $\mathbf{e}_j$ is a unit vector in the direction of the jth Cartesian axis. This gives

$$\Phi(\mathbf{m}+B^t\mathbf{e}_j)-\Phi(\mathbf{m}) = N\pi\mathbf{e}_j\cdot BA^t\cdot\mathbf{e}_j+2N\pi\mathbf{e}_j\cdot A^t\cdot\mathbf{m}+2\pi\left(A\mathbf{Q}_1-\frac{\mathbf{n}'}{2}\right)\cdot\mathbf{e}_j,$$
$$= N\pi(BA^t)_{jj}-\pi n'_j+2\pi l, \tag{A.47}$$

where l is an integer. In order that the sum over $\mathbf{m}$ in (A.42) is nonzero, the change in phase must be an integer multiple of 2π. Hence, the sum is nonzero only if

$$N(BA^t)_{jj}-n'_j=0 \mod 2 \quad \forall j\in\{1,\ldots,L\}. \tag{A.48}$$

The map is quantizable if $\psi(\mathbf{q}_2)$ is supported at points $\mathbf{Q}_2/N$ with $\mathbf{Q}_2\in Z^L$. This implies that each component of $\mathbf{n}'$ is even, and if the map is to be quantizable for all N we require

$$(AB^t)_{jj}=0 \mod 2 \quad \forall j\in\{1,\ldots,L\}. \tag{A.49}$$

We note that the number of integer points in $2B^t\square$ is $2^L\det B$. This leads to our final expression for h_N:

$$h_N(\mathbf{q}_2,\mathbf{Q}_1)=\frac{\det B}{N^L}\sum_{\mathbf{Q}_2\in Z^L}\delta^L\left(\mathbf{q}_2-\frac{\mathbf{Q}_2}{N}\right)$$
$$\times\left\langle\exp\left[\mathrm{i}\pi N\left(\mathbf{m}\cdot A^t(B^t)^{-1}\cdot\mathbf{m}+2\left(\frac{A\mathbf{Q}_1}{N}-\frac{\mathbf{Q}_2}{N}\right)\cdot(B^t)^{-1}\cdot\mathbf{m}\right)\right]\right\rangle_{\mathbf{m}}, \tag{A.50}$$

where the angle brackets denote averaging over integer vectors $\mathbf{m}$. Substituting this into (A.40) leads to

$$\psi(\mathbf{q}_2)=\sum_{\mathbf{Q}_2\in Z^L}\sum_{\mathbf{Q}_1\in N\square}U_{\mathbf{Q}_2,\mathbf{Q}_1}\Psi(\mathbf{Q}_1)\delta^L\left(\mathbf{q}_2-\frac{\mathbf{Q}_2}{N}\right), \tag{A.51}$$

with

$$U_{\mathbf{Q}_2,\mathbf{Q}_1}=\left(\frac{\mathrm{i}}{N}\right)^{L/2}\sqrt{\det B}\exp\left(\frac{\mathrm{i}\pi}{N}\left[\mathbf{Q}_1\cdot B^{-1}A\cdot\mathbf{Q}_1+\mathbf{Q}_2\cdot DB^{-1}\cdot\mathbf{Q}_2-2\mathbf{Q}_2\cdot(B^t)^{-1}\cdot\mathbf{Q}_1\right]\right)$$
$$\times\left\langle\exp\left(\mathrm{i}\pi\left[N\mathbf{m}\cdot B^{-1}A\cdot\mathbf{m}+2\mathbf{Q}_1\cdot B^{-1}A\cdot\mathbf{m}-2\mathbf{Q}_2\cdot(B^t)^{-1}\cdot\mathbf{m}\right]\right)\right\rangle_{\mathbf{m}}. \tag{A.52}$$

This is the quantization of the unperturbed map in L dimensions. This map has the property that $U_{\mathbf{Q}_2+N\mathbf{n},\mathbf{Q}_1}=U_{\mathbf{Q}_2,\mathbf{Q}_1}$. Hence, the transformed wavefunction may be written as

$$\psi(\mathbf{q}_2)=\sum_{\mathbf{Q}_2\in\square_N}\sum_{\mathbf{Q}_1\in\square_N}U_{\mathbf{Q}_2,\mathbf{Q}_1}\Psi(\mathbf{Q}_1)\langle\mathbf{q}_2|\mathbf{Q}_2\rangle. \tag{A.53}$$

This shows that the quantum propagator on the torus is equivalent to an $N^L\times N^L$ matrix transformation of the functions $\Psi(\mathbf{Q})$.

A.3. Perturbed cat maps

As shown by Keating [14], the arithmetic symmetries of cat maps lead to a non-generic spectrum. In [11, 34] these symmetries were removed by the addition of a small non-linear

perturbation of the map. The perturbation used was a shear in the momentum. An analogous perturbation for the hyperbolic toral automorphisms is

$$\rho\begin{pmatrix} q_1 \\ q_2 \\ p_1 \\ p_2 \end{pmatrix} = \begin{pmatrix} q_1 \\ q_2 \\ p_1 + \frac{k_1}{4\pi}\cos\ 2\pi q_1 \\ p_2 + \frac{k_2}{4\pi}\cos\ 2\pi q_2 \end{pmatrix}. \tag{A.54}$$

This perturbation is periodic under $\mathbf{q} \to \mathbf{q} + \mathbf{m}$, where $\mathbf{m}$ is an integer vector. The quantum propagator for this evolution may be found by considering the continuous-time evolution given by

$$\rho_t\begin{pmatrix} q_1 \\ q_2 \\ p_1 \\ p_2 \end{pmatrix} = \begin{pmatrix} q_1 \\ q_2 \\ p_1 + \frac{k_1 t}{4\pi}\cos\ 2\pi q_1 \\ p_2 + \frac{k_2 t}{4\pi}\cos\ 2\pi q_2 \end{pmatrix}. \tag{A.55}$$

This time evolution is generated by the Hamiltonian

$$H_{k_1,k_2} = -\frac{k_1}{8\pi^2}\sin\ 2\pi q_1 - \frac{k_2}{8\pi^2}\sin\ 2\pi q_2, \tag{A.56}$$

and consequently the evolution operator corresponding to (14), which is given by $\rho_{t=1}$, is

$$\langle \mathbf{q}|U|\mathbf{q}'\rangle = \delta^2(\mathbf{q}-\mathbf{q}')\exp\left[\frac{\mathrm{i}k_1\sin(2\pi q_1)}{8\pi^2\hbar}\right]\exp\left[\frac{\mathrm{i}k_2\sin(2\pi q_2)}{8\pi^2\hbar}\right]. \tag{A.57}$$

The quantum propagator acts on the basis $|\mathbf{Q}\rangle$ as

$$\langle \mathbf{q}|U|\mathbf{Q}\rangle = \sum_{\mathbf{Q}'\in\square_N}\langle \mathbf{q}|\mathbf{Q}'\rangle U_{\mathbf{Q}',\mathbf{Q}} \tag{A.58}$$

with

$$U_{\mathbf{Q}',\mathbf{Q}} = \delta_{\mathbf{Q},\mathbf{Q}'}\exp\left[\frac{\mathrm{i}Nk_1}{4\pi}\sin\left(\frac{2\pi Q_1}{N}\right) + \frac{\mathrm{i}Nk_2}{4\pi}\sin\left(\frac{2\pi Q_2}{N}\right)\right]. \tag{A.59}$$

References

[1] Berry M V 1977 Regular and irregular semiclassical wavefunctions *Phys. Rev.* A **10** 2083–91

[2] Blum G, Gnutzmann S and Smilansky U 2002 Nodal domain statistics: a criterion for quantum chaos *Phys. Rev. Lett.* **88** 114101

[3] Bogomolny E and Schmit C 2002 Percolation model for nodal domains of chaotic wave functions *Phys. Rev. Lett.* **88** 114102

[4] Elon Y, Gnutzmann S, Joas C and Smilansky U 2007 Geometric characterization of nodal domains: the area-to-perimeter ratio *J. Phys. A: Math. Theor.* **40** 2689–707

[5] Foltin G, Gnutzmann S and Smilansky U 2004 The morphology of nodal lines—random waves versus percolation *J. Phys. A: Math. Gen.* **37** 11363–71

[6] Aronovitch A and Smilansky U 2007 The statistics of the points where nodal lines intersect a reference curve *J. Phys. A: Math. Theor.* **40** 9743–70

[7] Bogomolny E and Schmit C 2007 Random wave functions and percolation *J. Phys. A: Math. Theor.* **40** 14033–43

[8] Bohigas O, Giannoni M J and Schmit C 1984 Characterization of chaotic quantum spectra and universality of level fluctuation laws *Phys. Rev. Lett.* **52** 1–4
[9] Keating J P, Marklof J and Williams I G 2006 Nodal domain statistics for quantum maps, percolation, and stochastic Loewner evolution *Phys. Rev. Lett.* **97** 034101
[10] Hannay J H and Berry M V 1980 Quantization of linear maps on a torus—Fresnel diffraction by a periodic grating *Physica* D **1** 267–90
[11] Keating J P, Mezzadri F and Monastra A G 2003 Nodal domain distributions for quantum maps *J. Phys. A: Math. Gen.* **36** L53–9
[12] Kesten H 1982 *Percolation Theory for Mathematicians. Progress in Probability and Statistics* (Boston, MA: Birkhäuser)
[13] Rivas A M F, Saraceno M and Ozorio de Almeida A M 2000 Quantization of multidimensional cat maps *Nonlinearity* **13** 341–76
[14] Keating J P 1991 The cat maps: quantum maps and classical motion *Nonlinearity* **4** 309–41
[15] Robinson C 1999 *Dynamical Systems: Stability, Symbolic Dynamics and Chaos (Studies in Advanced Mathematics)* 2nd edn (Boca Raton, FL: CRC Press)
[16] Hoshen J and Kopelman R 1976 Percolation and cluster distribution. I. Cluster multiple labelling technique and critical concentration algorithm *Phys. Rev.* B **14** 3438–45
[17] Ziff R M, Finch S R and Adamchik V S 1997 Universality of finite-size corrections to the number of critical percolation clusters *Phys. Rev. Lett.* **79** 3447–50
[18] Falconer K 2003 *Fractal Geometry: Mathematical Foundations and Applications* 2nd edn (New York: Wiley)
[19] Kurlberg P and Rudnick Z 2000 Hecke theory and equidistribution for the quantization of linear maps of the torus *Duke Math. J.* **103** 47–77
[20] Keating J P and Mezzadri F 2000 Pseudo-symmetries of Anosov maps and spectral statistics *Nonlinearity* **13** 747–75
[21] Keating J P 1991 Asymptotic properties of the periodic orbits of the cat maps *Nonlinearity* **4** 277–307
[22] Cardy J L 1992 Critical percolation in finite geometries *J. Phys. A: Math. Gen.* **25** L201–6
[23] Abramowitz M and Stegun I A 1974 *Handbook of Mathematical Functions* (New York: Dover)
[24] Anderson G D, Qiu S-L, Vamanamurthy M K and Vuorinen M 2000 Generalized elliptic integrals and modular equations *Pac. J. Math.* **192** 1–37
[25] Schramm O 2000 Scaling limits of loop-erased random walks and uniform spanning trees *Israel J. Math.* **118** 221
[26] Smirnov S 2001 Critical percolation in the plane: Conformal invariance, Cardy's formula, scaling limits *C. R. Acad. Sci. Paris* I **333** 239–44
[27] Bernard D, Boffetta G, Celani A and Falkovich G 2006 Conformal invariance in two-dimensional turbulence *Nat. Phys.* **2** 124–8
[28] Marshall D E and Rohde S 2006 Convergence of the Zipper algorithm for conformal mapping *Preprint* math.CV/0605532
[29] Kager W, Nienhuis B and Kadanoff L P 2004 Exact solutions for Loewner evolutions *J. Stat. Phys.* **115** 805–22
[30] Gruzberg I A 2006 Stochastic geometry of critical curves, Schramm-Loewner evolutions and conformal field theory *J. Phys. A: Math. Gen.* **39** 12601–55
[31] Bogomolny E, Dubertrand R and Schmit C 2007 SLE description of the nodal lines of random wavefunctions *J. Phys. A: Math. Theor.* **40** 381–95
[32] Keating J P, Mezzadri F and Robbins J M 1999 Quantum boundary conditions for torus maps *Nonlinearity* **12** 579–91
[33] Marklof J 1999 Theta sums, Eisenstein series, and the semiclassical dynamics of a precessing spin *Emerging Applications of Number Theory, (IMA Volumes in Mathematics and its Applications)* vol 109 (New York: Springer) pp 405–50
[34] Basilio de Matos M and Ozorio de Almeida A M 1995 Quantization of Anosov maps *Ann. Phys.* **237** 46–65